Optimization of a multi-speckle setup and dynamical response in the covalent bonded glass-former B_2O_3

Author:
Boyan H. Kintov

Supervisors:
Prof. Dr. Paul H.M. van Loosdrecht
Prof. Dr. Giulio Monaco

September 30, 2015

Contents

1 Introduction

Disordered materials are characterized by a complex mechanical response related to the coexistence of dynamical processes taking place over multiple time and length scales. Despite the intense research effort undertaken during the last decades, several of their key properties still remain poorly understood. A common aspect of these materials is that, by varying some external parameter, they can usually undergo structural arrest, e.g. a glass can be obtained quenching a liquid below a temperature known as the glass transition temperature, T_g. Significantly, the understanding of the dynamics in disordered systems is very relevant in several scientific domains as, e.g., biology: in fact, globular proteins are colloids, DNA is a stiff polymer and the lipids forming cell membranes are essentially surfactants.

The aim of the present work is to use dynamic light scattering to investigate the dynamical response of the covalent bonded glass-former B_2O_3 both close to the structural arrest and in the arrested state. Dynamic light scattering is a widespread technique useful to investigate the dynamics in ergodic systems [BP76]. Its application close to the structural arrest or in the arrested state is, instead, more difficult. Some schemes based on multi-speckle detection using CCD cameras have been recently proposed to overcome these limitations [WW93], though only few experiments have been carried out up to now.

Within the present thesis, a multi-speckle setup will be installed and optimized at the Physics Department of the University of Trento to work on samples close to the structural arrest. The multi-speckle detection provides a crucial advantage in the dynamic light scattering, since it simultaneously measures the dynamics of many equivalent speckles. This fact allows increasing significantly the amount of collected data in a certain time period and thus enhancing the accuracy of the derived results. Nevertheless, studying the dynamics of a disordered system, we have to average over time as well as over the number of considered speckles. In ergodic systems the time and ensemble average are considered as equivalent but in systems out of equilibrium this is not more the case, so that the order of averaging over time and space becomes important [CW99]. Therefore, two different approaches to calculate the autocorrelation function are tested and described in the following in order to explore their advantages or disadvantages in various conditions.

The distributions and fluctuations of the measured quantities also provide important information about the studied system. Recent works have proposed dynamic light scattering techniques to investigate the dynamical heterogeneity in glassy systems [Dur05]. In the present thesis, an alternative approach to probe the dynamical heterogeneity is tested, investigating the variances of the autocorrelation parameters as a function of the measurement time.

In what follows, the dynamics of B_2O_3 as a function of temperature will be studied with the aid of a CCD-camera and the obtained results will be compared to these of previous works. Below the glass transition temperature ageing effects appear clearly and the change of relaxation time as a function of "experimental" (waiting) time in the ageing boron oxide will be discussed.

2 Theoretical background

2.1 Glass systems

2.1.1 Historical overview

Glasses are known since the prehistoric times. The natural glass obsidian was used to make knifes and arrow tips. The most antique objects made of glass were found in Egypt dating from 3000 BC. Methods of manufacturing glass were already discovered in Mesopotamia around 4500 BC. The production technique in Europe came from the civilizations of Mycenae and Crete. Glass blowing was probably invented in Phoenicia around 50 BC and spread by the Roman Empire in Europe. During the Middle Ages the art of colouring glass was developed stimulated by the church in England. Around the 10th century Venice became predominant in the world of glass and led to the art of the "Venice Crystal" produced in Murano. The book *Arte vetraria* by Neri was published in Pisa in 1612 and translated into many other languages giving an overview of the knowledge about glass at this time. The glass manufacturing spread over the whole Europe especially in England, France and Bohemia. By the end of the 18th century chemical discoveries based on the replacement of natural alkali by sodium from sea salts led to an industrial revolution in the glass fabrication. The introduction of mechanized processes revolutionized again the glass industry to the end of the 19th century.

The use of glass for optical purposes together with the technological progress induced a better physical and chemical understanding. Glass lenses were already known by the Greeks whose knowledge was transferred to the Arabic world. Eyeglasses were fabricated in Italy in 1280 and the first telescopes in Italy and Netherlands around 1590. A spectacular progress was achieved at the end of the 18th century when B_2O_3, P_2O_5 and numerous other oxides were systematically introduced thanks to the collaboration of Abbe, Schott and Zeiss in Jena, Germany. Zeiss maintained a monopoly in the production of optical glasses, in particular for microscopes, until the First World War.

The studies of various glasses with different properties led to a more generalized concept of the vitreous state defining it as a non-crystalline solid (Tammann,1930). The scientific approaches changed slowly from the first pure phenomenological research toward more and more structural studies. After the Second World War due to the stronger interactions between research and technology the blossoming period of the true glass sciences began. Besides classical applications such as for housewares, construction, lighting, chemical industry etc. many new techniques for glass utilization appeared like laser, optical fibres or energy transformation.

2.1.2 Classification of solids

Solid materials can be classified in structural terms into three distinct categories: *cristalline, fractal* and *amorphous.*

- **Crystals** are ordered solids. Their high symmetrical structure is characterized by their translational periodicity. Identical unit cells, containing one or more atoms, are stacked in space to form the (three-dimensional) crystal lattice.

- **Fractal** structures are characterized by their detailed self-similarity at every length scale(Fig.1). Well known natural fractals are cauliflower and broccoli. Real fractal solids are for example aerogels, synthetic porous materials with very low density.
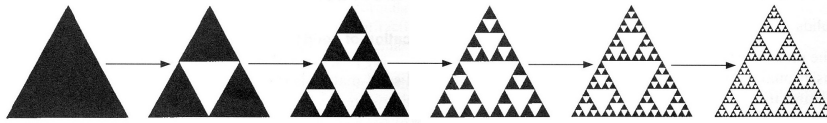

Figure 1: Sierpinski triangle [Ell00]

- **Amorphous** materials form a third general class of solids which don't exhibit neither the long range order like crystals nor the self-similarity of the fractals. Therefore they are also called disordered solids. However this does not mean a full absence of structure. In many cases, in particular for materials with predominantly covalent bonds, a short range order, characterized by coordination number, length and angle of the chemical bonds between the atoms, is well defined with only relative small statistical fluctuations. The resulting structure for a covalently bonded amorphous solid is called *continuous random network* (Fig.2a). Finally a non-crystalline material with a glass transition between the solid and liquid states is defined as glass.

The term *glass* usually denotes transparent and fragile materials. In scientific language this term includes a vast number of disordered materials thus it is more difficult to give an exact definition. Glass is essentially a non-crystalline solid obtained by cooling down a liquid but there are also other methods to realize it. Please note however that the term glass is also used as a synonym for a state of disorder. In fact we speak of *spin glass* to describe a magnetically disordered structure. In Fig.2 some types of disorder are shown.
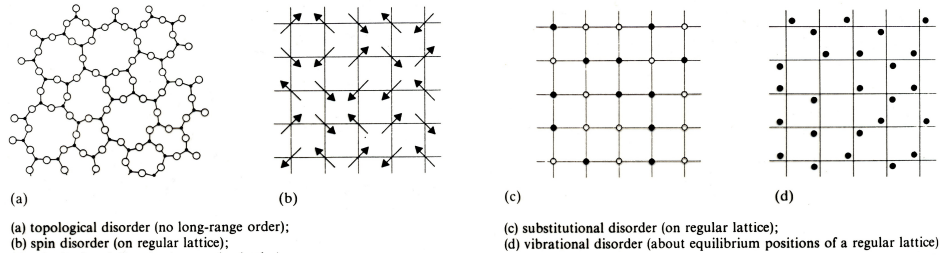
(a) topological disorder (no long-range order);
(b) spin disorder (on regular lattice);

(c) substitutional disorder (on regular lattice);
(d) vibrational disorder (about equilibrium positions of a regular lattice)

Figure 2: Types of disorder [Fon15]

2.1.3 Viscosity

The viscosity is a measure of the resistance of a fluid to gradually deform under a shear or tensile stress. The bulk viscosity describes the dissipative response of a system to a compression and plays a role in presence of rapid stress variation due e.g. to a sound or shock wave, while the shear (dynamic) viscosity originates from the friction forces between adjacent layers moving with different velocities.
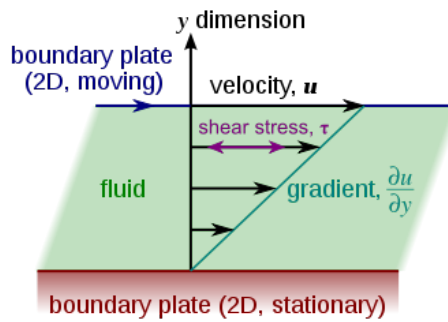

Figure 3: Laminar shear of fluid between two plates [Wik08]

If we decompose a force F acting on the surface S in its normal F_n and tangential F_t components respectively to S we can define the pressure (tension)

$$p = \frac{dF_n}{dS} \tag{1}$$

and the shear stress

$$\tau = \frac{dF_t}{dS} \ . \tag{2}$$

The tangential force required to move a plate over a liquid surface with a constant velocity is equal to the friction resistance of the liquid. The fluid particles adjacent to the plate move with the same velocity whereas those on the ground don't move at all. Thus the difference of the velocities between two adjacent liquid layers at a distance dy is expressed by

$$v(y + dy) - v(y) = \frac{1}{\eta}\frac{F_t}{S}dy = \frac{1}{\eta}\tau dy \tag{3}$$

7

and the **viscosity** is then defined as

$$\eta = \frac{\tau}{\nabla v} \ .$$

(4)

Its unit is the Poise $[\text{gcm}^{-1}s^{-1}]$.

2.1.4 Vitrification

Many materials, when melting, became liquids with low viscosity ($\sim 10^{-2}$ Poise). Such liquids crystallize rapidly when cooled below the melting point even at higher cooling rates. There are also substances with much higher viscosity in the liquid phase ($\sim 10^6$ Poise). Those liquids, if kept just below their melting point, will tend to slowly crystallize because the crystalline phase is from the thermodynamic point of view more stable than the supercooled liquid. If, instead, the liquid is cooled quickly enough the crystallization can be totally avoided because the viscosity increases gradually up to that of a solid ($\sim 10^{12}$ Poise). The continuous passage from a liquid to a solid suggests however similarities between the structures of both states. In Fig.4 the X-ray diffraction
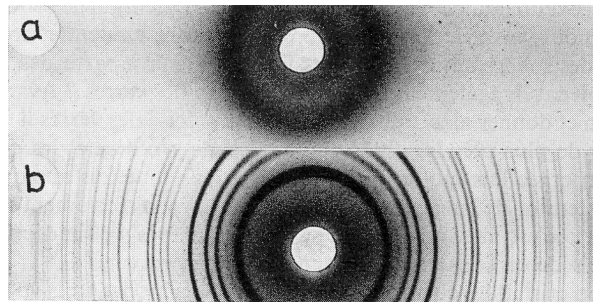

Figure 4: X-ray diffraction of silica glass(a) and cristobalite(b) [Zar82]

pattern of silica glass and its corresponding crystal cristobalite are shown. The few large blurred rings in (a) confirm the disordered structure of the glass whereas the numerous discrete thin lines in (b) are typical for the long-range order of polycrystalline substances.

The ability of a material to form a glass depends not only on the chemical composition but also on the cooling rate. Some substances cannot vitrify if they are not cooled sufficiently fast. For example some metal alloys need a cooling rate in the order of 10^6K/s to became glassy whereas others such as B_2O_3 cannot easily crystallize. The volume and mass are also important parameters for the vitrification.

Glasses can be formed not only by cooling of liquids but also from the gas or crystalline phase. The condensation of vapour on a wall at sufficiently low temperature can strongly reduce the mobility of the deposited atoms and lead to the formation of a disordered

structure. On the other hand it is also possible to obtain an amorphous solid by destroy-
ing the crystalline order. The radiation of α-particles or fast neutrons on a crystal causes
defects in the crystalline lattice by displacements of the atoms that can, accumulating,
lead to **amorphisation**. The effects of prolonged mechanical action may progressively
destruct the crystalline order as well. Similar effects can be quickly obtained by the
brutal impact of a shock wave (by bomb blast e.g.).

2.1.5 Vitreous state

The definition of the glassy state could be of pure operational type: *Glass is a disordered
solid obtained by cooling of liquid,* but we would exclude materials formed in other ways as
mentioned in the previous section. Another definition of structural type could include all
disordered solids implying that glass and non-crystalline, amorphous solid are synonyms,
but it wouldn't be satisfactory. Some non-crystalline materials remain disordered by
reversible temperature variation but show changes in their physical properties. Other
disordered substances like Si or Ge crystallize. We use the phenomenon of the *glass
transition* to differentiate them. Thus we can define the glassy state as a non-crystalline
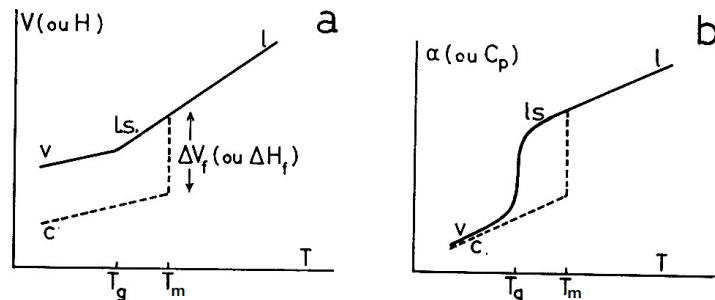solid that has a **glass transition**.

Figure 5: Dependence on the temperature of the volume(enthalpy)(a) and the expansion
coefficient(heat capacity)(b) [Zar82]

The classical way to obtain a glass is by rapidly quenching of a liquid to avoid the
crystallization. The continuous growth of the viscosity with decreasing temperature
leads to solidification. To better understand this process it is convenient to follow the
behaviour of some thermodynamic parameter such as the volume as a function of the
temperature in Fig.5. When the liquid approaches the melting point T_m, two events may
occur, either it crystallizes and causes a discontinuity in the volume variation ΔV_m (in
general a contraction) or the volume continues to change with the same slope crossing
T_m, in that case we speak of a *supercooled liquid*. In the first case the crystallized solid
continues to contract by cooling with a linear slope smaller than that in the liquid phase.
In the second case the supercooled liquid contracts with the same coefficient as before
but after a certain temperature T_g the slope decreases abruptly approaching that of the

9

crystal. T_g is the temperature of the glass transition at which the viscosity becomes very large of the order of 10^{13} poise. In Fig.5b the derivative of the volume is shown as function of the temperature.

The trend of the volume-temperature curve can be explained by the mechanism of the viscous relaxation. As long as the system is in the supercooled liquid domain it is able to instantly modify its molecular configuration by rotations and translations of its molecules and to achieve a quasi-equilibrium at the various temperatures. The rate of such structural modifications depends on temperature and decreases strongly with it. When the rate of the configuration variation becomes of the same order as the cooling rate, the system is no more able to follow the variation of the external conditions and a deviation in the curve slope is observed at T_g where it occurs. Because the structural evolution below T_g is not in the quasi-equilibrium we do not speak any more of supercooled liquid but use the term glass.
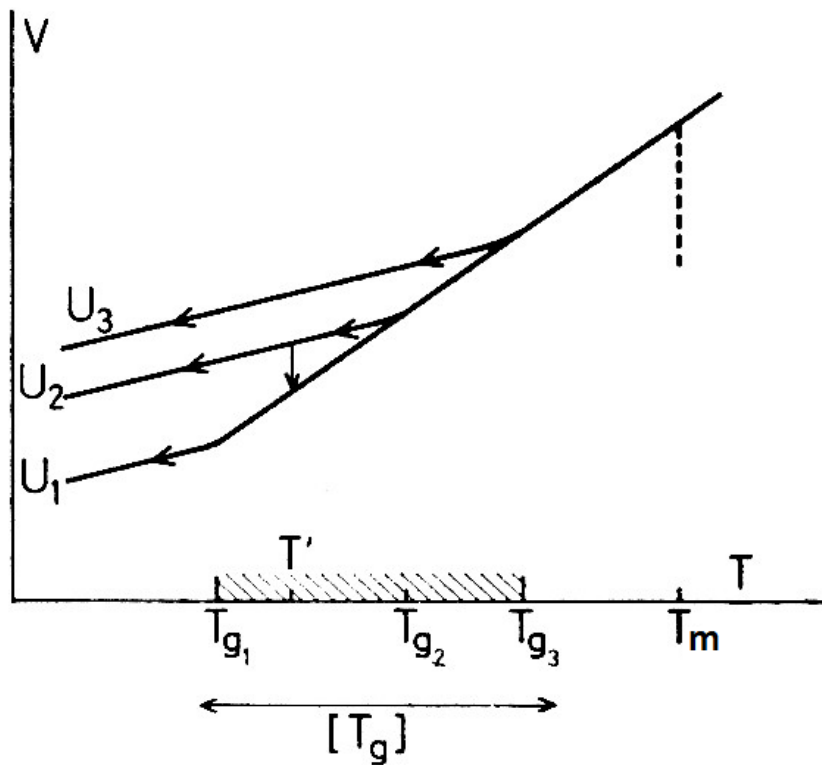

Figure 6: Influence of the cooling rate($U_1 < U_2 < U_3$) on the glass transition [Zar82]

As shown in Fig.6 the exact position of the transition point T_g is not unique but depends on the cooling rate. It makes sense, therefore, to speak rather of transition range. A slower cooling tends to shift T_g to lower temperatures thus leading to the important conclusion that the physical properties of the glass depend on its thermal history.

The thermodynamic parameters temperature and pressure are not sufficient to define the

vitreous state, because of its non-equilibrium conditions, therefore we need an additional one to characterize the configuration of the system. A widely used parameter is the **fictive temperature** T_f introduced by Tool(1946). A glass has the fictive temperature T_f if its configuration corresponds to that in its "liquid equilibrium" at this temperature. For a supercooled liquid T_f is simply its current temperature whereas for a glass $T_f = T_g$ as in Fig.6. Reheating a glass to another temperature in the glass transition range it will tend to achieve the equilibrium changing its structural configuration and thus its fictive temperature.

2.1.6 Thermodynamics of the glass system

The dependence of the glass transition on temperature requires the consideration of some thermodynamic variables such as *enthalpy, entropy* and *heat capacity*.

- The **enthalpy** of a system is defined by

$$H = E + PV \tag{5}$$

  where E is the internal energy, P the pressure and V the volume of the system. The enthalpy variation of a reaction at a constant pressure is thus given by

$$\Delta H = \Delta E + P\Delta V \ . \tag{6}$$

  If there are no phase transitions or the volume does not change, the variation of enthalpy is nothing else than that of the internal energy. Finally $\Delta H = Q$ where Q is the exchanged heat between the system and environment.

- The **entropy** is an extensive property and commonly understood as the degree of disorder of the system. It measures the amount of work needed to obtain an ordered system. For heat exchange between the system and its environment at a constant temperature the variation of the system's entropy is given by

$$\Delta S = \frac{Q}{T} \ . \tag{7}$$

- The **heat capacity** is the amount of heat needed to raise the system's temperature by one Kelvin. At constant pressure it is defined as

$$C_p = \left(\frac{\partial H}{\partial T}\right)_p \ . \tag{8}$$

The volume variation is entirely analogous to that of the enthalpy, thus its derivative C_p will be equivalent to α (Fig.5). At the melting point T_m the enthalpy jump corresponds

to the **latent heat of fusion** L_f. In the vitrification process the curve of C_{pl} passes continuously T_m and decreases rapidly at T_g tending to that of the crystal C_{ps} (Fig.7a).

Using eqs. (7) and (8) we can write the entropy variation

$$dS = \frac{C_p dT}{T} \tag{9}$$

and visualize it as the area under C_p which is a function of the temperature. Integrating
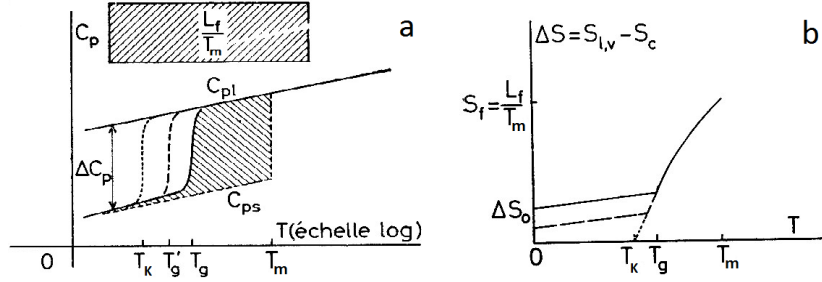

Figure 7: (a) C_p vs. $\log T$ (b) Kauzmann paradox [Zar82]

both C_{pl} and C_{ps} in Fig.7a for the liquid-glass transition respectively for the crystallized solid we can calculate the entropy difference between crystalline solid and supercooled liquid

$$\Delta S = \frac{L_f}{T_m} - \int_0^{T_m} (C_{pl} - C_{ps}) \frac{dT}{T} \tag{10}$$

where $\frac{L_f}{T_m}$ is the entropy variation given by the latent heat of fusion L_f at the melting point T_m. The experience shows that this difference is not zero thus the glass have an excess of entropy compared to the crystal.

Fig.7b shows ΔS as a function of temperature. During the cooling the system tries to reduce ΔS but it is blocked in the vicinity of T_g. If we extrapolate the curve of ΔS it will cut the T-axis at T_K, the Kauzmann temperature, where the entropy of the supercooled liquid becomes equal to that of the crystal ($\Delta S = 0$). This leads to the paradox that below T_K the supercooled liquid would have lower entropy than that of the crystal thus at the absolute zero the entropy would become even negative in contradiction to the third law of the thermodynamics. To eliminate this problem we have to introduce T_K as the thermodynamic limit for the glass transition.

2.1.7 Fragility

The viscosity of a supercooled liquid increases very fast below the melting temperature and achieves such high values that the system can be considered practically as solid.

Conventionally T_g is defined as the temperature at which the viscosity $\eta = 10^{13}$poise. Experimentally it has been shown that in many cases the viscosity in the vicinity of T_g follows the *Vogel-Fulcher* law

$$\eta(T) = Ae^{\frac{B}{T-T_0}} \tag{11}$$

where the parameters A, B and T_0 depending on the considered system; when $T_0 = 0$ it has the so called *Arrhenius* behaviour. Referring to the dependence of the viscosity on temperature we distinguish two types of glass: *strong* and *fragile*. In strong glasses the viscosity varies essentially in an Arrhenius manner as a function of T^{-1}, whereas in fragile glasses it significantly deviates from this trend(Fig.8).
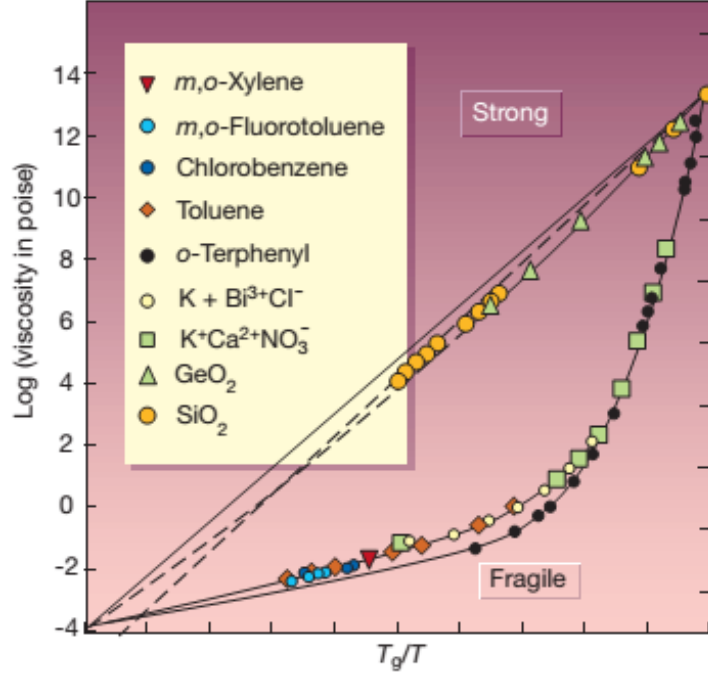

Figure 8: Arrhenius plot of the viscosity in strong and fragile glasses [Deb01]

The slope of the viscosity curve close to T_g defines the **fragility** index:

$$m = \left.\frac{\mathrm{d}\log_{10}\eta(T)}{\mathrm{d}(T_g/T)}\right|_{T=T_g}. \tag{12}$$

Its values varies from ~ 10 in strong glasses up to about 150 for fragile systems. Notice please that the fragility is a dimensionless quantity defined by the common logarithm providing thus more convenient scaling of the y-axis.

2.1.8 Viscoelastic relaxation

The response of a glass system to a mechanical stress depends on the stress duration and on the temperature of the system.

13

At sufficiently low temperatures the glass acts as a totally elastic solid following Hooke's law that establishes a proportionality between the external stress and the elastic strain. In Fig.9a the applied tangential force F on the surface S of a body with length L causes
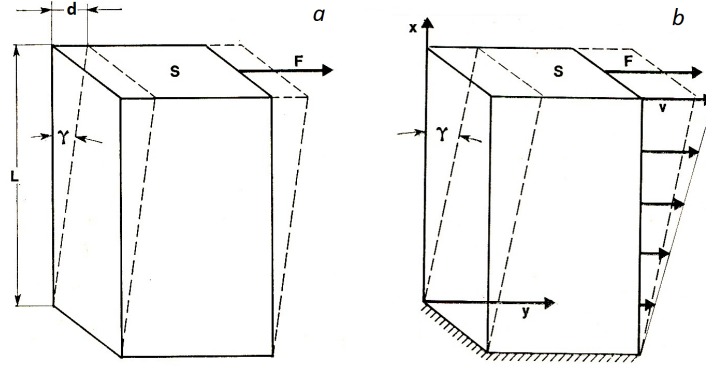

Figure 9: (a)elastic strain   (b)viscous creep [Fon15]

the elastic *shear* deformation

$$\frac{d}{L} = \tan \gamma_e \approx \gamma_e \tag{13}$$

where γ is small enough to satisfy Hooke's law

$$\tau = \frac{F}{S} = G\gamma_e \tag{14}$$

with the elasticity constant G. The elastic deformation is reversible i.e. the system recovers completely its initial form after the external force is removed.

At temperatures above the transition range the system acts as a viscous *Newtonian fluid* as discussed in 2.1.4. The shear stress is proportional to the velocity gradient (Fig.9b)

$$\tau = \eta\frac{dv}{dx} = \eta\frac{d\gamma_v}{dt} \tag{15}$$

where we used in the second identity

$$\frac{dv}{dx} = \frac{d}{dx}\left(\frac{dy}{dt}\right) = \frac{d}{dt}\left(\frac{dy}{dx}\right) = \frac{d\gamma_v}{dt} \; .$$

In contrast to the elastic case the viscous deformation is permanent i.e. it is irreversible.

In the vicinity of the glass transition the system has the so called *viscoelastic* behaviour which can be explained applying the *Maxwell model*. In presence of a constant external stress the initially pure elastic strain is followed by the gradually viscous deformation of

14

the system. The total strain is then simply given by the sum of both distinct deformations

$$\gamma_{tot} = \gamma_e + \gamma_v = \frac{\tau}{G} + \frac{\tau}{\eta} t \ . \tag{16}$$

The relative contributions of the elastic and viscous components can be expressed by the time needed for the viscous deformation to equal the elastic strain

$$\frac{\tau}{G} = \frac{\tau}{\eta} t_r \ .$$

Thus the so called **relaxation time** is defined by

$$t_r = \frac{\eta}{G} \ . \tag{17}$$

The rapid quench of a liquid below its T_g causes microscopical internal tensions in the material. Those can be removed by reheating the system and maintaining it sufficiently long at temperatures near the glass transition. This *relaxation process* is essentially the conversion of the initially elastic strain into the permanent viscous deformation. Using eqs. (15) and (16) under the constraint that the total deformation γ_{tot} of the system is constant we obtain

$$0 = \frac{d\gamma_{tot}}{dt} = \frac{d\gamma_e}{dt} + \frac{d\gamma_v}{dt} = \frac{1}{G}\frac{d\tau}{dt} + \frac{\tau}{\eta}$$

The solution of this equation gives a simple qualitative formulation of the relaxation process

$$\tau = \tau_0 e^{-\frac{G}{\eta}t} = \tau_0 e^{-\frac{t}{t_r}} \ . \tag{18}$$

Relaxation processes are in general more complicated due to retarded elasticity caused by imperfections in the structure or due to variation of the viscosity with time. In many experimental applications it is thus necessary to adjust empirically the above relation.

2.2 Dynamic light scattering

2.2.1 Introduction

Electromagnetic radiation is one of the most important experimental tools that can provide, depending on the wavelength, detailed information about complex structures and dynamics of matter. Different techniques like X-ray diffraction, Raman or absorption spectroscopy have been developed to examine the translational, rotational, vibrational and electronic degrees of freedom as well as the composition of solids and biological macromolecules. On the following we will treat the characteristics of light scattered from rotational and translational degrees of freedom known as *Rayleigh scattering*.

When light impinges on matter the electric field induces oscillations of the constituent charged particles such as electrons, ions or dipole molecules which subsequently radiate (scatter) the absorbed light acting as secondary sources. The frequency variation, the angular distribution, the polarization and the intensity of the scattered light gives then information about molecular size, shape and interaction in the scattering medium.

In a light-scattering experiment a monochromatic laser beam is focussed on a sample and its scattered light is registered from a detector at angle θ with respect to the transmission direction (Fig.10). The intersection between transmitted and scattered beam defines
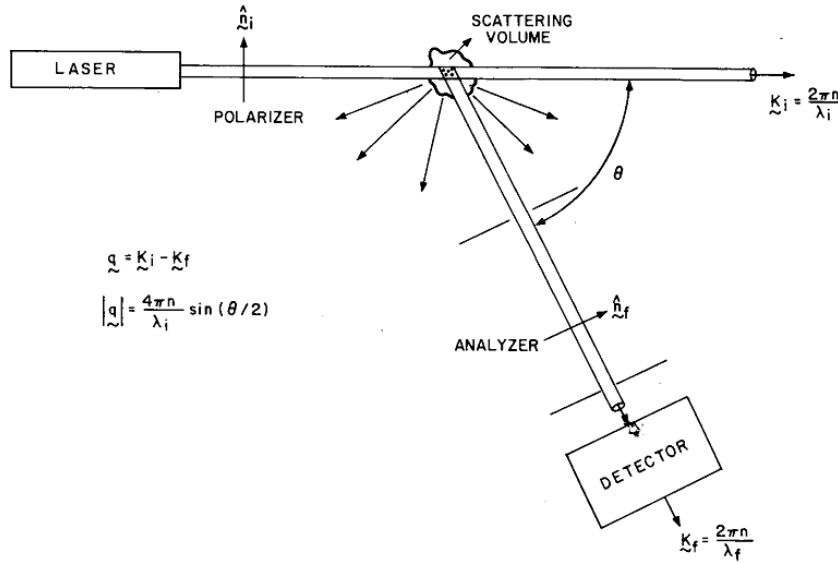

Figure 10: Scheme of a scattering experiment [BP76]

the *illuminated* or *scattering volume*. In an idealized model the incident light is a plane electromagnetic wave

$$\mathbf{E}_i(\mathbf{r}, t) = \mathbf{n}_i E_0 e^{i(\mathbf{k}_i \mathbf{r} - \omega_i t)} \tag{19}$$

16

of frequency ω_i, polarisation $\mathbf{n}_i$, amplitude E_0 and wave vector $\mathbf{k}_i$. The constituent charges of the molecules in the illuminated volume are accelerated by the incident field and radiate light according to classical electrodynamics. The scattered light registered from the detector at a given instant is the superposition of the radiated fields from all charges in the scattering volume thus it depends on their exact positions. However, the charges are permanently in thermal motion so that the registered field at the detector will randomly vary and will look like a noise pattern. Therefore we will need some concepts from the noise theory and stochastic processes to extract information.

2.2.2 Fluctuations and time correlation

In light scattering experiments the incident field is sufficiently weak to assume a linear response of the system so that its dynamical variables can be completely described in terms of time correlation functions.

We consider a property A that depends on the positions and momenta of all molecules in the system such as the pressure in a gas closed in a container. The particles are randomly moving around and are hitting against the container's walls. The resulting force acting on the walls at a given instant will depend on the momentum transferred by the molecules and will fluctuate with time. Hence the exact instantaneous pressure defined as $\frac{\text{force}}{\text{surface}}$ will fluctuate in time too. It is then reasonable to average over sufficiently long time T compared to the period of the fluctuations

$$\bar{A}(t_0, T) = \frac{1}{T} \int_{t_0}^{t_0+T} dt A(t) \tag{20}$$

where t_0 is the initial time. In the ideal case A should be averaged over an infinite time

$$\langle A \rangle = \lim_{T \to \infty} \frac{1}{T} \int_0^T dt A(t) \tag{21}$$

to obtain a time independent mean value. A property with an average that does not depend on the initial value is called *stationary property*.

The noise signal A in Fig.11 can in general have different values at times t and $t + \tau$

$$A(t) \neq A(t + \tau) .$$

When τ is very small compared to the fluctuation period, $A(t + \tau)$ will be very close to $A(t)$ so that we can say they are correlated. A measure of this correlation is given by the **autocorrelation function** of A

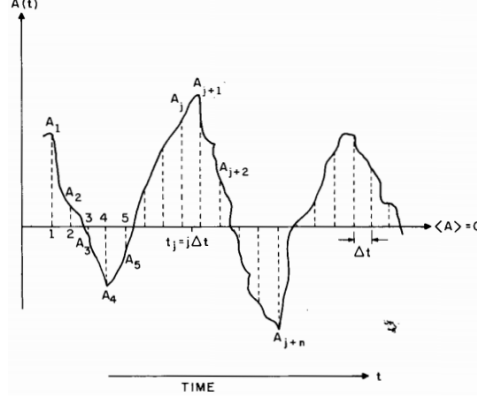$$\langle A(0)A(\tau) \rangle = \lim_{T \to \infty} \frac{1}{T} \int_0^T dt A(t) A(t + \tau) \tag{22}$$

17

Figure 11: Fluctuations of the property A(t) [BP76]

In a real experiment the property A will be measured for small discrete time intervals Δt so that the equations (21) and (22) can be respectively approximated by the sums

$$\langle A \rangle = \lim_{N \to \infty} \frac{1}{N} \sum_{j=1}^{N} A_j \tag{23}$$

$$\langle A(0)A(\tau) \rangle = \lim_{N \to \infty} \frac{1}{N} \sum_{j=1}^{N} A_j A_{j+n} \tag{24}$$

where we substituted $t = j\Delta t, \tau = n\Delta t$ and $T = N\Delta t$.

Without loss of generality we can assume $\langle A \rangle = 0$ and evaluate the dependence on time of the autocorrelation function. Since the fluctuations are around zero some terms in the sum (24) will be negative. Consider first the case $\tau = 0$. All terms in

$$\sum_{j=1}^{N} A_j A_j = \sum_{j=1}^{N} A_j^2$$

will be positive and the total value will become large. For $\tau > 0$ there will be some cancellations due to the negative contributions implying that

$$\langle A(0)^2 \rangle \geq \langle A(0)A(\tau) \rangle . \tag{25}$$

This indicates that the autocorrelation function either remains constant for all times τ i.e. it is a conserved quantity or decays from its initial value which is the maximum. For large τ, compared to the characteristic time of the fluctuations, $A(t)$ and $A(t + \tau)$ are expected to become totally uncorrelated

$$\lim_{\tau \to \infty} \langle A(0)A(\tau) \rangle = \langle A(0) \rangle \langle A(\tau) \rangle = \langle A \rangle^2 \tag{26}$$

so that the autocorrelation function of a non periodic property A decays from $\langle A^2 \rangle$ to $\langle A \rangle^2$ as shown in Fig.12.
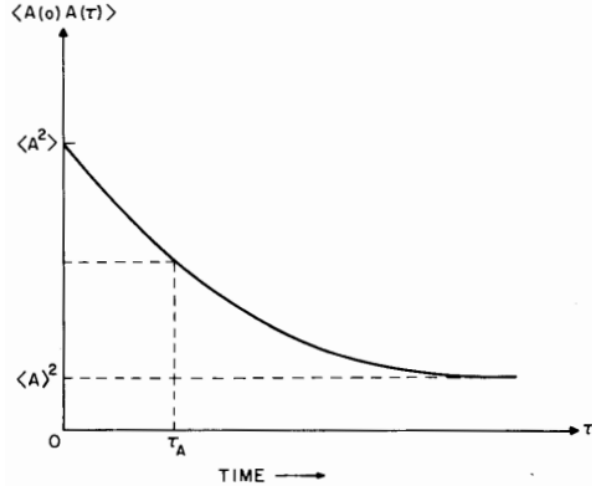
Figure 12: Decay of the autocorrelation function $\langle A(0)A(\tau)\rangle$ [BP76]

In many applications the autocorrelation function decays like a single exponential

$$\langle A(0)A(\tau)\rangle = \langle A\rangle^2 + \left[\langle A^2\rangle - \langle A\rangle^2\right]e^{-\frac{\tau}{\tau_r}} \tag{27}$$

where τ_r is the characteristic decay time of A called *correlation time* or also *relaxation time*.

If we define the instantaneous deviation of $A(t)$ from its mean value

$$\delta A(t) \equiv A(t) - \langle A\rangle \tag{28}$$

it is easy to show by substitution in eq.(22) that

$$\langle \delta A(0)\delta A(\tau)\rangle = \langle A(0)A(\tau)\rangle - \langle A\rangle^2 \tag{29}$$

and

$$\langle \delta A^2\rangle = \langle A^2\rangle - \langle A\rangle^2 \ . \tag{30}$$

From eqs. (27),(29) and (30) it follows

$$\langle \delta A(0)\delta A(\tau)\rangle = \langle \delta A^2\rangle e^{-\frac{\tau}{\tau_r}} \ . \tag{31}$$

Not all autocorrelation functions decay exponentially. The correlation time is thus defined as

$$\tau_c \equiv \int_0^\infty d\tau \frac{\langle \delta A(0)\delta A(\tau)\rangle}{\langle \delta A^2\rangle} \ . \tag{32}$$

where $\tau_c = \tau_r$ for the exponential case. In general the correlation time is some complicated function of many relaxation processes contributing to the decay of δA.

In real systems (glasses e.g.) the relaxation time τ_r can become so large that it will be impossible to perform a measurement long enough for a satisfactory time averaged autocorrelation function. Therefore in systems of many identical particles it will be reasonable to employ the **ensemble average**. Systems which produce the same results by averaging over time as well as over (phase) space are called **ergodic systems**.

The instantaneous state of a mechanical system is completely specified by its generalized coordinates $(q_1, ..., q_f)$ and momenta $(p_1, ..., p_f)$ given as a point $\mathbf{\Gamma}_t \equiv [\mathbf{q}(t), \mathbf{p}(t)]$ in the $2f$-dimensional phase space at any time t. The time evolution is then represented as a trajectory in the phase space which, for ergodic systems and for $t \to \infty$, will completely explore the phase space volume. Hence a mechanical property A of the system can be defined as a function of its generalized coordinates $A(t) \equiv A(\mathbf{\Gamma}_t)$ and its ensemble-averaged autocorrelation function is then

$$\langle A(0)A(t) \rangle \equiv \int d\mathbf{\Gamma}_0 \rho(\mathbf{\Gamma}_0) A(\mathbf{\Gamma}_0) A(\mathbf{\Gamma}_t) \tag{33}$$

where the product $A(\mathbf{\Gamma}_0)A(\mathbf{\Gamma}_t)$ depends on t and $\rho(\mathbf{\Gamma}_0)d\mathbf{\Gamma}_0$ gives the probability to find the system in the state $\mathbf{\Gamma}_0$.

2.2.3 Spectral density

In scattering experiments the spectral density or *power spectrum* is the measured quantity defined as the time Fourier transform of the autocorrelation function

$$I_A(\omega) \equiv \frac{1}{2\pi} \int_{-\infty}^{+\infty} dt\, e^{-i\omega t} \langle A^*(0)A(t) \rangle \ . \tag{34}$$

Using the inverse Fourier transform

$$\langle A^*(0)A(t) \rangle = \int_{-\infty}^{+\infty} d\omega\, e^{i\omega t} I_A(\omega)$$

we find for $t = 0$ the mean-square value of A

$$\langle |A|^2 \rangle = \int_{-\infty}^{+\infty} d\omega\, I_A(\omega) \tag{35}$$

where $d\omega I_A(\omega)$ can be interpreted as the amount of $|A|^2$ in the frequency interval $(\omega, \omega + d\omega)$.

2.2.4 Light scattering

We consider a plane wave

$$\mathbf{E}_i(\mathbf{r}, t) = \mathbf{n}_i E_0 e^{i(\mathbf{k}_i \mathbf{r} - \omega_i t)} \tag{36}$$

which passes through a transparent, non-magnetic and non-conducting medium with refractive index $n = \sqrt{\varepsilon_0}$. The incident field will induce oscillations in the charge density thus the local dielectric constant will fluctuate too. From the Maxwell equations an expression can be derived of the scattered field in terms of the dielectric fluctuation

$$E_s(R,t) = \frac{-k_f^2 E_0}{4\pi R \varepsilon_0} e^{i(k_f R - \omega_i t)} \delta\varepsilon_{if}(\mathbf{q}, t) \tag{37}$$

where k_f is the scattered wave number, ω_i the initial field frequency and R the distance from the scattering volume[BP76]. The dielectric fluctuation tensor

$$\delta\varepsilon_{if}(\mathbf{q}, t) \equiv \mathbf{n}_f \cdot \delta\boldsymbol{\varepsilon}(\mathbf{q}, t) \cdot \mathbf{n}_i \tag{38}$$

depends on the polarizations of the incident and scattered field $\mathbf{n}_i$ and $\mathbf{n}_f$ respectively, as well as on the exchanged momentum $\mathbf{q} = \mathbf{k}_i - \mathbf{k}_f$. Supposing that $|\mathbf{k}_i| = |\mathbf{k}_f|$ we can express the magnitude of $\mathbf{q}$ by the Bragg condition

$$|\mathbf{k}_i - \mathbf{k}_f| = q = \frac{4\pi n}{\lambda} \sin\frac{\theta}{2} \tag{39}$$

where θ is the scattering angle between $\mathbf{k}_i$ and $\mathbf{k}_f$ as shown in Fig.13.

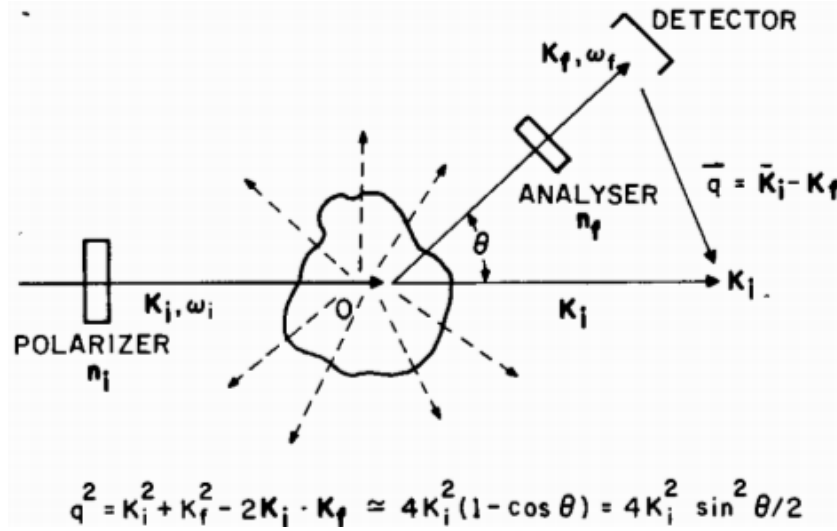$$q^2 = K_i^2 + K_f^2 - 2K_i \cdot K_f \simeq 4K_i^2(1 - \cos\theta) = 4K_i^2 \sin^2\theta/2$$

Figure 13: Scattering geometry [BP76]

The autocorrelation function of the scattered electric field is thus given by

$$\langle E_s^*(R,0) E_s(R,t) \rangle = \frac{k_f^4 |E_0|^2}{16\pi^2 R^2 \varepsilon_0^2} \langle \delta\varepsilon_{if}(\mathbf{q},0) \delta\varepsilon_{if}(\mathbf{q},t) \rangle e^{-i\omega_i t} \tag{40}$$

and the spectral density by its Fourier transform

$$I_{if}(\mathbf{q}, \omega_f, R) = \left[\frac{I_0 k_f^4}{16\pi^2 R^2 \varepsilon_0^2}\right] \frac{1}{2\pi} \int_{-\infty}^{+\infty} dt \langle \delta\varepsilon_{if}(\mathbf{q},0) \delta\varepsilon_{if}(\mathbf{q},t) \rangle e^{i(\omega_f - \omega_i)t} \tag{41}$$

21

where we substituted $I_0 \equiv |E_0|^2$. Note that the power spectrum depends on the frequency change $\omega = \omega_i - \omega_f$. The dependence on k^4 explains why longer waves are less scattered and the dependence on R^{-2} represents the expected attenuation for a spherical wave. If however $\delta\varepsilon(\mathbf{q}, t)$ does not depend on time the integral in (41) would yield $\delta(\omega_i - \omega_f)$ and there would be no frequency shift. Scattering can occur from "frozen" fluctuations but incident and scattered wave would have the same frequency (Rayleigh scattering).

The Fourier transform of the autocorrelation function of the dielectric fluctuations is then

$$I_{if}^{\varepsilon}(\mathbf{q}, \omega) = \frac{1}{2\pi} \int_{-\infty}^{+\infty} dt \langle \delta\varepsilon_{if}^*(\mathbf{q}, 0) \delta\varepsilon_{if}(\mathbf{q}, t) \rangle e^{-i\omega t} . \tag{42}$$

and it is proportional to the scattered intensity $I_{if}(\mathbf{q}, \omega_f, R)$ with the proportionality constant

$$A = \frac{I_0 k_f^4}{16\pi^2 R^2 \varepsilon_0^2} .$$

Analogous results can be derived considering the induced dipole moments of the single molecules in the scattering medium

$$\boldsymbol{\mu}_j(t) = \boldsymbol{\alpha}_j \cdot \mathbf{E}_i(t) . \tag{43}$$

We assume that the molecules are electronically weakly coupled i.e. not much disturbed by their neighbours and we neglect any collision effects. The scattered field can be then derived from the theory of the dipole radiation and will be thus proportional to the sum of the contributions from each molecule in the illuminated volume

$$E_s(t) \sim \sum_j \alpha_{if}^j(t) e^{i\mathbf{q}\cdot\mathbf{r}_j(t)} \tag{44}$$

where $\mathbf{r}_j(t)$ is the translation of the j-th molecule and the time dependent **polarizability tensor**

$$\alpha_{if}^j(t) = \mathbf{n}_f \cdot \boldsymbol{\alpha}(t) \cdot \mathbf{n}_i \tag{45}$$

expresses its rotations and vibrations relative to the incident and scattered field polarizations. Due to the relation $\varepsilon = 1 + 4\pi\alpha$ thus $\delta\varepsilon = 4\pi\delta\alpha$ the spectral density will be proportional to

$$I_{if}^{\alpha}(\mathbf{q}, \omega) = \frac{1}{2\pi} \int_{-\infty}^{+\infty} dt \langle \delta\alpha_{if}^*(\mathbf{q}, 0) \delta\alpha_{if}(\mathbf{q}, t) \rangle e^{-i\omega t} \tag{46}$$

where

$$\delta\alpha_{if}(\mathbf{q}, t) = \sum_j^N \alpha_{if}^j(t) e^{i\mathbf{q}\cdot\mathbf{r}(t)} \tag{47}$$

is the spatial Fourier component of the polarizability density

$$\delta\alpha_{if}(\mathbf{r}, t) = \sum_j^N \alpha_{if}^j(t) \delta(\mathbf{r} - \mathbf{r}_j(t)) . \tag{48}$$

2.2.5 Optical mixing

The output of the detector, usually a photomultiplier tube, is proportional to the intensity of the scattered light (or number of photons) thus to the squared electromagnetic field $i(t) \sim |E(t)|^2$. The output current $i(t)$ is then passed into a computer (or correlator), which calculate the autocorrelation function

$$\langle i(0)i(t) \rangle = B \langle |E(0)|^2 |E(t)|^2 \rangle \tag{49}$$

where B is a proportionality constant. We distinguish two methods of detecting or *optical mixing*:

- In the **homodyne** method only the scattered light impinges on the detector and we define the *homodyne autocorrelation function* of the scattered intensity

$$I_2(t) \equiv \langle |E_s(0)|^2 |E_s(t)|^2 \rangle \ . \tag{50}$$

- In the **heterodyne** method a local oscillator, usually a small portion of the unscattered laser beam, is mixed with the scattered light. The autocorrelation function of the output becomes

$$\langle i(0)i(t) \rangle = B \langle |E_{LO}(t) + E_s(t)|^2 |E_{LO}(0) + E_s(0)|^2 \rangle \ . \tag{51}$$

Assuming that the fluctuations of $E_{LO}(t)$ are negligible and both $E_{LO}(t)$ and $E_s(t)$ are statistically independent, eq.(51) reduces to [BP76]

$$\langle i(0)i(t) \rangle \cong B \left[I_{LO}^2 + 2I_{LO}ReI_1(t) \right] \tag{52}$$

where $I_{LO} = \langle |E_{LO}|^2 \rangle$ and $ReI_1(t)$ the real part of the *heterodyne autocorrelation function*

$$I_1(t) \equiv \langle E_s^*(0)E_s(t) \rangle \ . \tag{53}$$

Under certain conditions the homodyne correlation function $I_2(t)$ can be expressed in terms of $I_1(t)$. In the *Gaussian approximation* the illuminated volume is considered as divided in many small subregions so that the scattered field can be expressed as the sum of independent Gauss-distributed random variables

$$E_s = \sum_n E_s^{(n)} \tag{54}$$

where $E_s^{(n)}$ is the scattered field from the n-th subregion. In the Gaussian distribution all higher moments are related to the first two moments thus it can be shown that the fourth moment $I_2(t)$ is related to the second moment $I_1(t)$ trough the expression [BP76]

$$I_2(t) = |I_1(0)|^2 + |I_1(t)|^2 \ . \tag{55}$$

Important for this approximation is that all subregions are statistically independent and sufficiently large to satisfy the central limit theorem.

In general the homodyne autocorrelation function contains more information than the heterodyne one, because additional terms can appear.

2.2.6 Autocorrelation function for particle diffusion

We consider a simplified system of independent identical spherical particles as an approximation for dilute suspensions of macromolecules e.g. According to eq.(45) the polarizability tensor of the particles is given by

$$\alpha_{if}^{j}(t) = \alpha \mathbf{n}_f \cdot \mathbf{n}_i \tag{56}$$

where α is the constant isotropic polarizability of the particle j. Its fluctuations follow from eq.(47)

$$\delta\alpha_{if}(\mathbf{q}, t) = \alpha \mathbf{n}_f \cdot \mathbf{n}_i \sum_{j}^{N} e^{i\mathbf{q}\cdot\mathbf{r}(t)} \tag{57}$$

where the sum goes over all particles in the scattering volume. The function

$$F_1(\mathbf{q}, t) = \langle \psi^*(\mathbf{q}, t)\psi(\mathbf{q}, t) \rangle \tag{58}$$

with

$$\psi(\mathbf{q}, t) = \sum_{j}^{N} e^{i\mathbf{q}\cdot\mathbf{r}(t)}$$

is proportional to the heterodyne autocorrelation function in eq.(53). Assuming that the particles move independently, thus have independent positions $\mathbf{r}_j(t)$, F_1 simplifies to the *self-correlation* function

$$F_1(\mathbf{q}, t) = \left\langle \sum_{j=1}^{N} b_j(0)b_j(t)e^{i\mathbf{q}\cdot[\mathbf{r}_j(t)-\mathbf{r}_j(0)]} \right\rangle \tag{59}$$

where

$$b_j(t) = \begin{cases} 1 & j \in V \\ 0 & j \notin V \end{cases}$$

counts the particles remaining in the scattering volume V at time t. In typical light scattering experiments the characteristic time τ_v needed by a particle to leave the scattering volume V is given by

$$\tau_v = \frac{L^2}{D}$$

24

with D the diffusion coefficient of the system and $L \sim 0.01\mathrm{cm}$ the typical length scale of the illuminated volume. In contrast the particle displacements $[\mathbf{r}_j(t)-\mathbf{r}_j(0)]$ contributing to the sum in eq.(59) are of the order of $q \sim 10^5\mathrm{cm}^{-1}$ with characteristic times

$$\tau_q = \frac{1}{q^2 D} \ .$$

Comparing both time scales

$$\frac{\tau_v}{\tau_q} = (qL)^2 \sim 10^6$$

we see that $b_j(0)b_j(t)$ varies much slower than $\exp\left(i\mathbf{q} \cdot [\mathbf{r}_j(t) - \mathbf{r}_j(0)]\right)$ and we can approximate

$$b_j(0)b_j(t) \simeq b_j(0)b_j(0) = b_j(0)$$

where the last identity comes from the fact that $b_j(0)$ is either 0 or 1. We can thus write

$$F_1(\mathbf{q},t) = \langle N \rangle F_s(\mathbf{q},t)$$

where

$$F_s(\mathbf{q},t) \equiv \langle e^{i\mathbf{q}\cdot[\mathbf{r}_j(t)-\mathbf{r}_j(0)]} \rangle \tag{60}$$

is the so called *self-intermediate scattering function*. Its spatial Fourier transform is the *van Hove function*

$$G(\mathbf{R},t) = \langle \delta(\mathbf{R} - [\mathbf{r}_j(t) - \mathbf{r}_j(0)]) \rangle$$

which describes the probability that the particle moves over distance R in time t and can be regarded as a solution of the diffusion equation

$$\frac{\partial}{\partial t}G(\mathbf{R},t) = D\nabla^2 G(\mathbf{R},t) \ . \tag{61}$$

The spatial Fourier transform of this equation

$$\frac{\partial}{\partial t}F_s(\mathbf{q},t) = -q^2 D F_s(\mathbf{q},t) \tag{62}$$

has the solution

$$F_s(\mathbf{q},t) = e^{-q^2 Dt} \tag{63}$$

with the relaxation time $\tau_q = (q^2 D)^{-1}$ as introduced above. It follows that the heterodyne autocorrelation function is given by the exponentially decaying function

$$F_1(\mathbf{q},t) = \langle N \rangle e^{-q^2 Dt} \tag{64}$$

and in the Gaussian approximation we obtain according to eq.(55) the homodyne autocorrelation function

$$F_2(\mathbf{q},t) = \langle N \rangle^2 + \langle N \rangle^2 e^{-2q^2 Dt} \ . \tag{65}$$

Substituting the *Einstein relation*

$$D = \frac{k_B T}{6\pi\eta a}$$

for the diffusion coefficient, we can e.g. measure the radius a of the diffusing particles if we know the viscosity η at temperature T of the solvent.

2.2.7 Coherence area

The concept of *coherence area* is central in optical mixing experiments. When light impinges on a screen the produced diffraction pattern, i.e. the intensity maxima and minima, depends on the extent L of the light source (Fig.14). Since each point of the source radiates incoherently, i.e. with a random phase, the intensity at point A on the screen will result as a superposition of the waves from all points of the source. If point B is very close to A, the intensity will be almost identical to that in A thus we could say both signals are correlated or *coherent* to each other. The distance at which the space correlation function $\langle E(A)E(B) \rangle$ of the signals at A and B differs significantly from zero is formally defined as *coherence distance*.
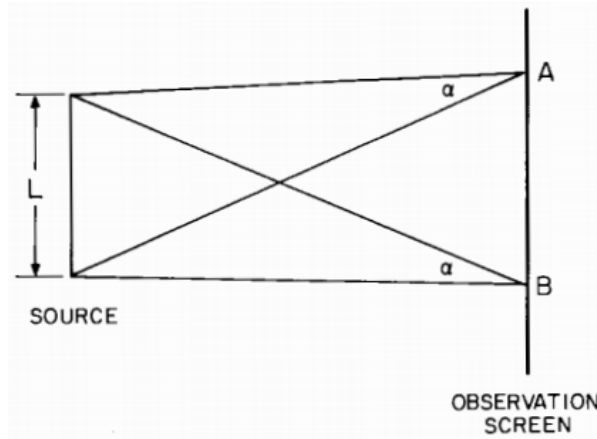

Figure 14: Coherence area [BP76]

It may be shown by computing of $\langle E(A)E(B) \rangle$ that the distance over which the signals at A and B are correlated is approximately

$$l_c \approx \frac{\lambda}{\alpha} \tag{66}$$

where α is the resulting angle from the extent of the source on the screen and λ the wavelength of the light [BP76]. If we observe a two dimensional flat screen the area around the point A at which the signals are spatially correlated is defined as the **coherence area** A_{coh}. An estimate of A_{coh} is given by

$$A_{coh} \approx \frac{\lambda^2}{\Omega} \tag{67}$$

where Ω is the solid angle of the source subtended at the screen.

3 Experiment

3.1 Sample preparation

Diboron trioxide is a typical glass forming material consisting mostly of planar BO_3-triangles, which build a disordered covalent bonded network. Pure B_2O_3 crystallizes very hardly even at the crystal melting temperature (450°C for trigonal B_2O_3) due to its high viscosity. Under normal conditions it adsorbs water molecules from the air humidity forming in a nontransparent white cover on its surface. To avoid this problem we melted directly the granular boron oxide of 99% purity produced by Sigma-Aldrich in cylindrical silica glass tubes 7mm in diameter and 1mm in thickness. Fused silica has similar optical properties as B_2O_3 but higher glass transition temperature ($\sim$ 1200°C) allowing thus to prepare transparent airtight samples.

Because of its hygroscopy the samples have been first dried for about 2 hours at 300°C evaporating in this way the adsorbed water molecules from the surface. After that they were slowly heated up to 900°C with a rate of 5°C/min to avoid any stress damages of the silica tube. The samples were then kept for several hours at 900°C to get rid of eventual bubbles and any remaining water (or hydroxyl ion) content. The sample A was held at 900°C for 12 hours, the samples B and C for 48 hours respectively. Subsequently the samples were slowly cooled down to 300°C with a rate of 5°C/min and then immediately placed in the furnace, where the measurements were performed at different temperatures near the glass transition.

Care had to be taken when cooling below the glass transition ($<$ 250°C). Once solidified the samples could not be reheated due to the very different thermal expansion coefficients of B_2O_3 ($\sim 10^{-4}$K^{-1} [Bot07]) and that of the enclosing silica glass ($\sim 10^{-6}$K^{-1} [Whi73]). For this reason the measurements were performed on cooling down the sample in steps of 5°C or 10°C. Important is also the remaining water content which reduces significantly the glass transition temperature T_g even if present at few percent level ($<$ 5%) as reported by Ramos et al. [Ram96]

3.2 Setup

For the measurements a coherent green laser light has been used of the wavelength $\lambda = 532$nm and power $P = 240mW$. To avoid oversaturation of the detector the beam has first been filtered to $\sim$ 3% of the primary intensity as reported in Fig.15, then focused on the sample by a lens of focal length $f = 25$cm to a focal spot of $\approx 100\mu$m. The sample was placed in a furnace with a temperature control to within 0.1°C. The furnace has four apertures at angles of 90° for the incoming, transmitted and at 90°

scattered beams. The scattered light was first selected by an aperture of 6 mm width, which was calculated to obtain speckles of similar size as the CCD-pixel size. The scattering volume of the sample is imaged through a lens of focal length $f = 15$cm on the CCD with a magnification $\frac{b}{g} = 1$ according to the *thin lens formula*

$$\frac{1}{f} = \frac{1}{g} + \frac{1}{b}$$

with the distances from the lens $b = g = 30$cm of the image and of the sample, respectively. In order to reduce any undesirable effects of external stray light the CCD-camera was enclosed in a dark box. All measures were performed in a dark room.
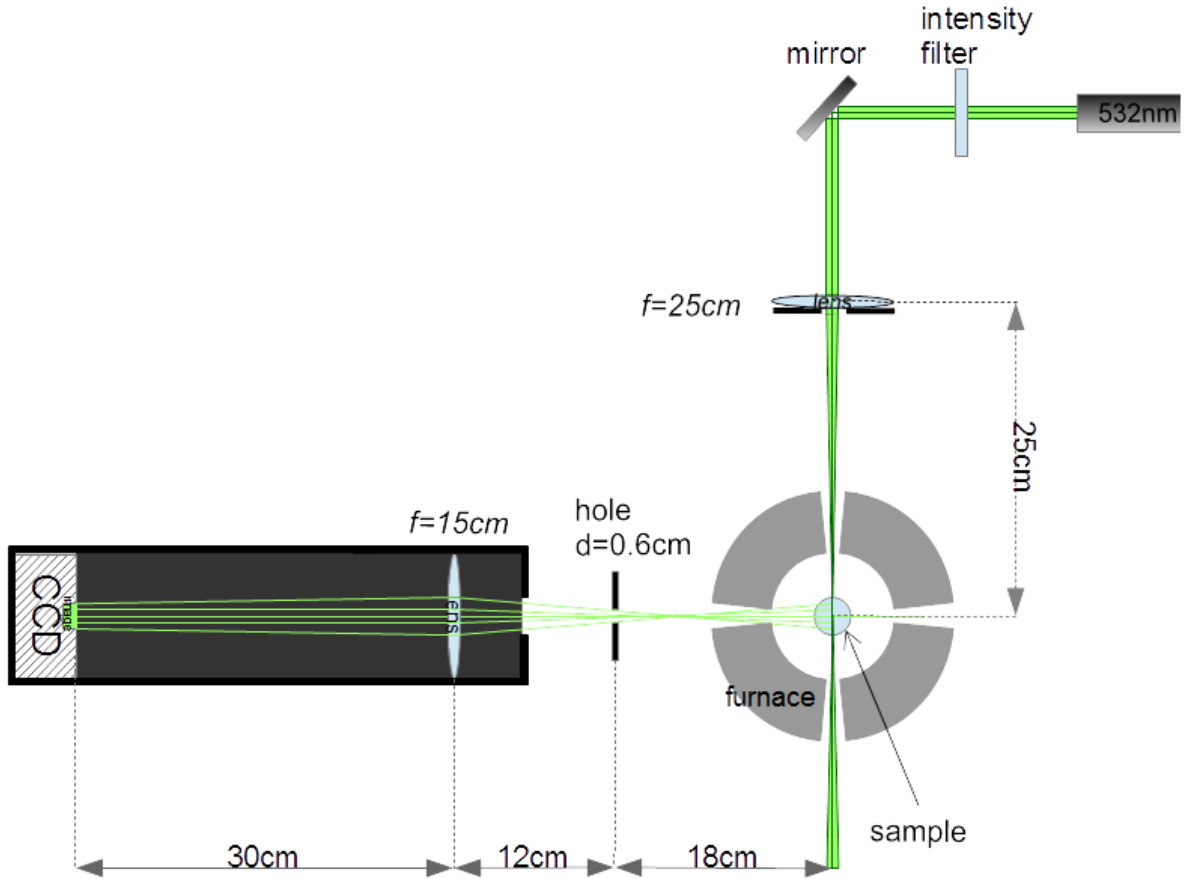
Figure 15: Experimental setup

The pixels of the CCD camera have the width of 9μm and the coherence area (speckle size) is given by

$$A_{coh} \approx \pi \left(\frac{\lambda D}{2d}\right)^2$$

where λ is the wavelength and D the distance from the sample to the pinhole of diameter d. The latter formula is derived by the geometry of our setup as shown schematically

in Fig.16. The speckle pattern on the CCD appears from the "source" of extent L on the lens over the distance b so that the speckle size or the diameter of a single coherence area results to

$$l \approx \frac{\lambda}{\alpha} \approx \frac{\lambda L}{b} = \frac{\lambda L}{g} = \frac{\lambda D}{d}$$

as introduced in section 2.2.7. Assuming the speckles are circles-like we obtain the coherence area by
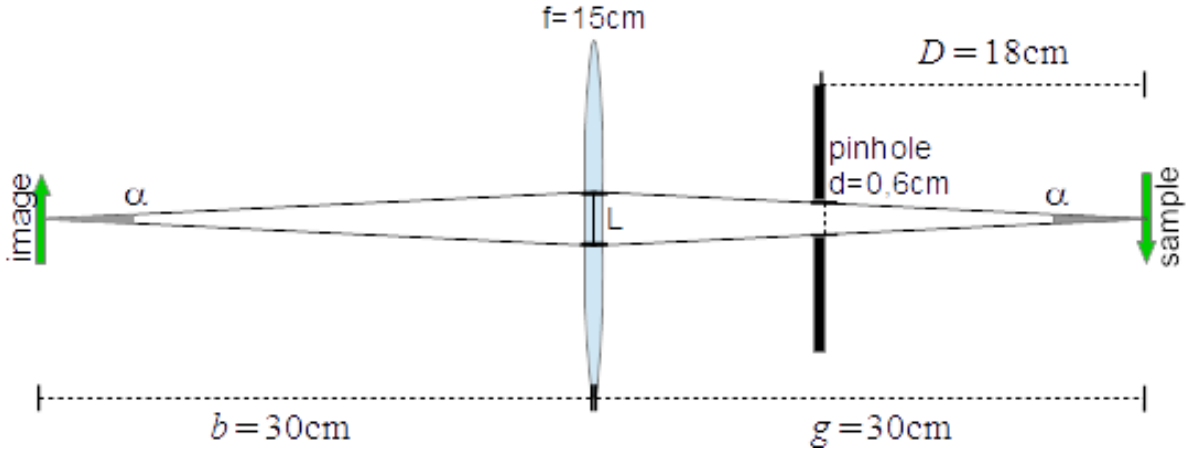
$$A_{coh} = \pi r^2$$

with

$$r = \frac{l}{2} = \frac{\lambda D}{2d} \quad .$$

Figure 16: Geometry of the speckle imaging

3.3 Measurement and evaluation

The measurements were performed on three samples at different temperatures mostly made with decreasing steps of 5°C or 10°C. After changing the temperature the system needed about 15min to achieve its thermal equilibrium before beginning with the measurements. The used CCD-camera has a recording rate of about 1 frame every second so that we could not measure relaxation times less than few seconds at temperatures far above the glass transition. At lower temperatures instead the relaxation time becomes very large so that it was necessary to perform long measurements to obtain satisfactory statistics. However the length of the measurements was limited to within one day and the longest one ($\sim$ 20000 frames) became even a challenge for computation of the large amount of data loaded at once. After each measurement the dark counts of the CCD-camera were recorded by covering the CCD aperture for about 20 frames.

3.3.1 Intensity distribution

In Fig.17 a typical speckle pattern is reported for an arbitrary frame recorded by the CCD. The beam enters from the left of the image and exits on the right side. It is evident that the speckle intensities are not homogeneous, i.e. the intensity decreases from the image middle to the borders below and above, where the speckles are almost no more visible and the signal decreases gradually to the dark noise. In order to keep the amount of data to a manageable level we cut all "dark" pixels, i.e. those of low intensity, as well as those strongly illuminated by reflections from the sample sides or its brass holder. However the *beam profile* and the *stray light* have significant contributions to the autocorrelation function which we will discuss later.
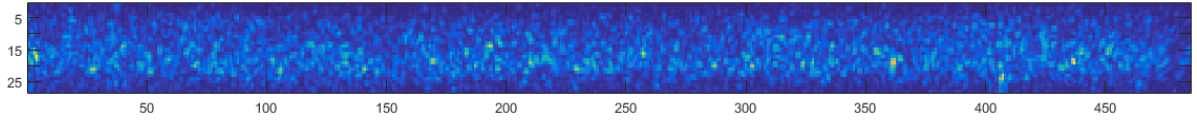

Figure 17: Typical intensity distribution of a frame recorded by the CCD-camera

The size of the image has a length of ~ 500 pixels that corresponds to $\sim 4{,}5$mm of the visible scattered beam length. That means that about 1mm on each side of the sample with diameter 7mm is cut from the image since the intensity scattered by the sample sides is dominated by stray light. The width of 25 pixels($= 225\mu$m) is close to the focal spot of $\approx 100\mu$m that explains also the gradually decreasing beam intensity profile.

The intensity distribution is described by the *Rayleigh statistics* with the exponential probability density

$$P(I) = \frac{1}{\langle I \rangle} \exp\left(-\frac{I}{\langle I \rangle}\right) \tag{68}$$

where $\langle I \rangle$ is the mean intensity [DC15].

Fig.18 represents a histogram of the pixel intensities computed over all 1461 frames from a measurement made at $T = 280°$C. The fitted exponential function coincides very well with the measured data for higher intensities. The most probable value of the Rayleigh distribution should be $I = 0$ that we could not observe due to the always present noise background. Consequently for low intensities the measured intensity distribution deviates significantly from the exponential shape and is additionally somewhat shifted toward higher intensities. The latter explains also the difference of both fit parameters $a = (9.13 \pm 0.05) \cdot 10^{-4}$ and $b = (-4.55 \pm 0.01) \cdot 10^{-4}$ whose absolute values should be equal to the reciprocal mean intensity

$$\tilde{a} = -b = \frac{1}{\langle I \rangle} \ .$$

In the picture is also shown the vertical straight line which cuts the fitted exponential curve at $y = 4.559 \cdot 10^{-4} \approx |b|$ where the ordinate should be shifted accordingly to

30

eq.(68). The red line traverses the data distribution near its maximum corresponding to the most probable measured intensities suggesting thus an estimate of the total intensity background. Due to the normalization of both data distribution and fitted exponential function by definition, the area of the data on the left from the red line is equal to the difference between the areas under the green fit and the data on the right side.
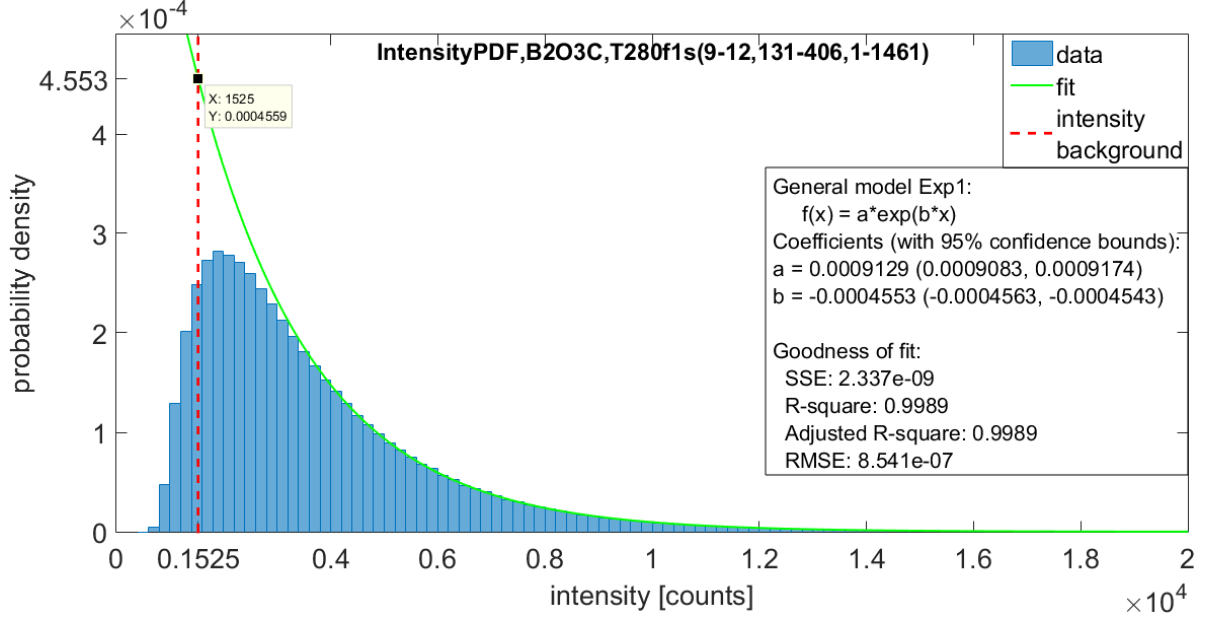

Figure 18: Probability distribution of the pixel intensities

The sequence of all frames from one measurement can be converted to a movie visualizing in this way the dynamic of the speckle pattern. At high temperatures above T_g the speckles move very fast, appearing and disappearing with the characteristic rate given by the relaxation time, whereas at low temperatures below T_g they move very slow and the pattern seems to be quasi static. The probability distribution of the intensity at different times has the same shape as in Fig.18 and the intensity histogram of an arbitrary pixel over the whole measurement time will be perfectly fitted by the same exponential function (with the same parameters) as above.

The time evolution of the intensity recorded by an arbitrary pixel at $T = 280°C$ is shown in Fig.19. The intensity peaks correspond to the appearing speckles and their widths to the relaxation time $\tau \approx 3s$ at this temperature. The red dashed line indicates the intensity background at ≈ 1500 counts as estimated in Fig.18 and the magenta dotted line shows the mean intensity of the signal. The reciprocal difference between signal mean and background intensity

$$(3700 - 1500)^{-1} \approx 4.5 \cdot 10^{-4}$$

corresponds approximately to the fit parameter $|b| = (4.55 \pm 0.01) \cdot 10^{-4}$ from Fig.18. However the origin of the background intensity is not trivial and was not the aim of this
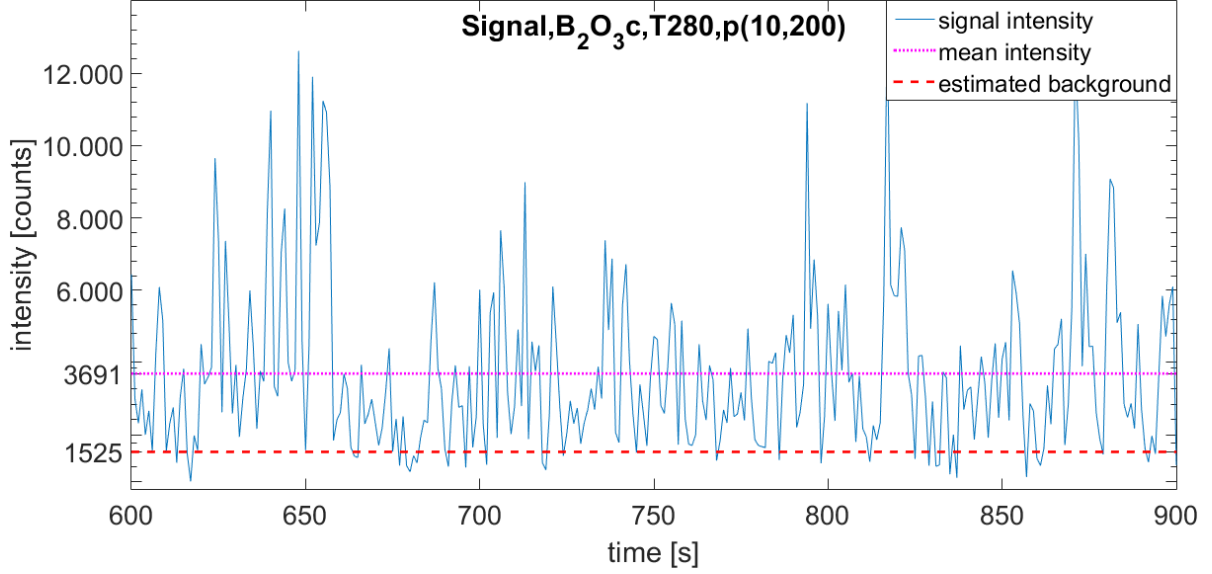
Figure 19: Intensity of an arbitrary pixel in time

work. Since it is surely composed of measurable contributions of the electronic noise and stray light the intensity distribution may also be influenced by the ratio speckle to pixel size as well as by the beam intensity profile.

3.3.2 Amplitude of the autocorrelation function and non ergodicity factor

We tested two different methods to treat the raw data. In both cases the dark counts data collected after each measurement were first subtracted in order to reduce the noise contribution to the CCD and the influence of eventual defected pixels. The autocorrelation function is then computed by averaging over time and space where the sequence of the averaging plays a central role.

By the *time averaging* method we computed first the time averaged autocorrelation function of each single pixel then the mean over all pixels

$$\langle C^p(t) \rangle_p = \left\langle \left\langle \frac{(I_f^p - \langle I^p \rangle_f)(I_{f+t}^p - \langle I^p \rangle_f)}{\langle I^p \rangle_f^2} \right\rangle_f \right\rangle_p \tag{69}$$

where I_f^p is the intensity of the p-th pixel and the f-th frame recorded by the CCD camera. The brackets express the average over all frames f and all pixels p respectively. Expanding the expression in the brackets we obtain the Siegert relation

$$C(t) = \frac{\langle I_f \cdot I_{f+t} \rangle}{\langle I \rangle^2} - 1 = |g(q,t)|^2 \quad . \tag{70}$$

32

In general the *self-intermediate scattering function* $g(q,t)$ is defined as the time Fourier transform of the dynamic structure factor $S(q,\omega)$ and depends also on the scattering angle. Because the latter was fixed at $90°$ the very small q-dependence will be further neglected.

As shown above $g(t)$ is directly proportional to the (heterodyne) autocorrelation function of the charge (density) fluctuations in the scattering medium and is assumed as the sum of many single exponential functions, i.e. of many relaxation processes. In the practice $g(t)$ is empirically approximated by the stretched exponential function

$$g(t) = \sqrt{C_0} \cdot e^{-(t/\tau)^\beta} \ . \tag{71}$$

Consequently the measured autocorrelation function is given by

$$C(t) = C_0 \cdot e^{-2(t/\tau)^\beta} \tag{72}$$

where C_0, τ and β are the fitting parameters in which we are interested.

The amplitude or *contrast* C_0 gives the initial value of the autocorrelation function and is related to the so called *non ergodicity level* f_0 of the scattering medium. This has been studied in detail within the *mode-coupling theory*. The theory predicts a two step relaxation for liquids: the main α and the fast β. Consider a jammed system of hard spheres such as the molecules in a (supercooled) liquid. The molecules will rattle in the cage formed by their neighbours and this motion will result in the so called fast β-relaxation of the autocorrelation function. The β-relaxation is always present even for solids at very low temperatures and depends strongly on q due to the *Debye–Waller—factor* $\sim \exp(-\frac{1}{3}q^2 u^2)$, where u is comparable with the cage extent, since it describes the average displacement of the molecules from their equilibrium positions. Characteristic times of various fast relaxations are reported in the range of 10^{-12}s - 10^{-2}s [Sid93].

The slow or main α-relaxation is related to the particle diffusion in liquids, that is when a molecule escapes from its cage. This depends strongly on the viscosity thus on the temperature of the liquid. At very low temperatures below T_g the viscosity and the relaxation time "diverges" to infinity, so that the glass is stuck in a non equilibrium state and the autocorrelation function decays to f_0, where it remains. In other terms the non ergodicity level gives the initial value of the α-relaxation.

In our experiment the contrast C_0 measures the mean squared intensity which is affected by two additional factors: an instrumental factor A_{coh} and a factor related to the stray light f_{st} so that

$$C_0 = f_0^2 A_{coh} f_{st} \ . \tag{73}$$

To demonstrate this the autocorrelation functions measured on B_2O_3 at $270°$C by photomultiplier and CCD are plotted together in Fig.20. The photomultiplier tube is able to measure very short relaxation times to the point that the tail of a faster relaxation

process is also visible in Fig.20. However it measures only one speckle at a time and longer measurements are more likely to be corrupted by sudden intensity distortions as when a dust particle crosses the laser beam e.g. On the other hand the CCD measurement is limited by the acquisition rate of 1 frame/s. The two detectors could be used simultaneously to measure the relaxation time only in a tight range of few seconds corresponding to temperatures $280 - 260°C$ of B_2O_3, where in particular the fit function of the CCD data is less precise due to the rare data points at short times.
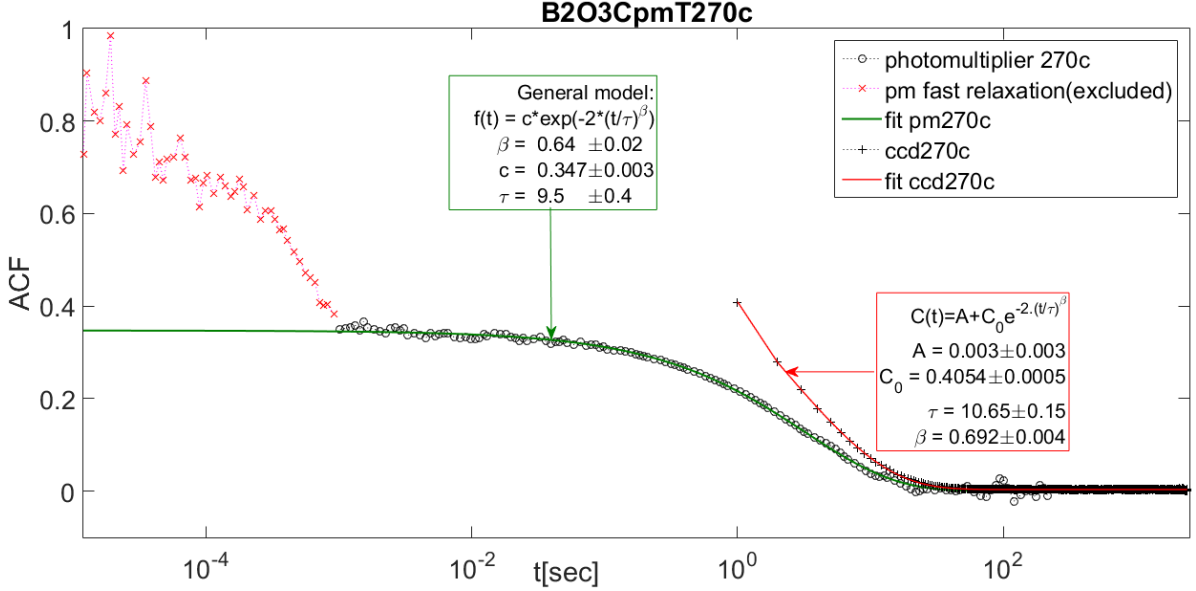
Figure 20: Autocorrelation function of boron oxide at $270°C$ measured by the photomultiplyer (circles). For comparison the data measured by the CCD (crosses) at the same temperature are plotted as well.

However both measurements give comparable results regarding τ and β but differ significantly in the contrast C_0. This can be explained by the different coherence (instrumental) factors A_{ccd} and A_{pm}. The photomultiplier factor could be measured by light scattering on the standard sample of colloidal polystyrene spheres of diameter $1\mu m$ in water and is given by $A_{pm} = 0,82 \pm 0,03$. Due to the short time limitation of the CCD its coherence factor A_{ccd} had to be calculated by comparison with the photomultiplier

$$A_{ccd} = A_{pm} \cdot \frac{C_{ccd}}{C_{pm}} = 0.96 \pm 0.03 \tag{74}$$

where C_{ccd} and C_{pm} are the measured contrasts of the CCD and the photomultiplier respectively at the same temperature of $270°C$. This result is reasonable since our speckles are of size ≈ 4 pixel thus the mean intensity registered by a single pixel correspond nearly to the real scattered intensity (dark counts are previously subtracted). If instead the coherence area is smaller than a pixel the mean intensity relative to the constant background and thus the contrast will be lower.
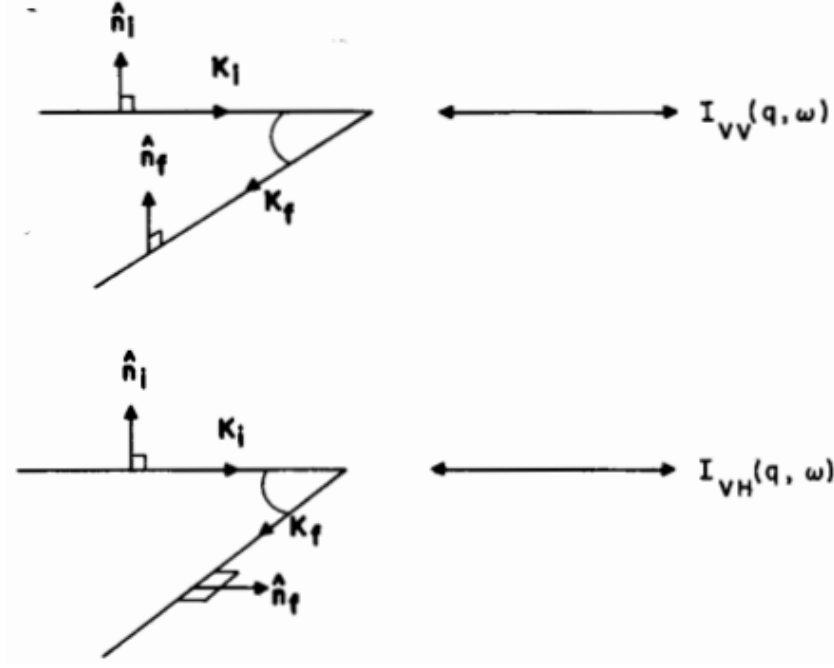
Figure 21: Polarization schemes in a scattering geometry [BP76]

The stray light correction factor to the contrast was calculated using the fact that the stray light has the same polarization as the incident laser beam. In Fig.21 the geometry of two different polarization schemes in a scattering process is schematically shown with the wave vectors K_i, K_f and the polarizations n_i, n_f of the initial and final wave respectively. If a linearly (vertically) polarized incoming beam is scattered on a disordered scattering medium the scattered light will have both a polarized and depolarized component. The scattered light can be separated in two components: E_{VV} the light scattered with the same polarization as the incoming (vertically polarized) beam and E_{VH} the light with 90°C rotated polarization. Both components should give the same contrast $C_0(= \langle I^2 \rangle)$ of the autocorrelation function. The stray light instead origins mostly from reflections of the environment or of "macroscopic" dust particles in the sample and has the polarization of the incident beam. Consequently it will raise the contribution of I_{VV} and reduce the contrast of the corresponding autocorrelation. To correct our data an additional measurement at 270°C was performed by using a polarization filter crosswise to the incoming laser polarization. The measured autocorrelation contrast is $C_0^{VH} = 0.65 \pm 0.02$ so that the stray light factor results

$$f_{st} = \frac{C_0}{C_0^{VH}} = 0.65 \pm 0.03$$

allowing together with A_{ccd} to calculate the non ergodicity factor f_0.

3.3.3 Time average

We return to the time averaging method of the autocorrelation function given by

$$\langle C^p(t)\rangle_p = \left\langle \left\langle \frac{(I^p_f - \langle I^p\rangle_f)(I^p_{f+t} - \langle I^p\rangle_f)}{\langle I^p\rangle^2_f} \right\rangle_f \right\rangle_p .$$

In Fig.22 the normalized autocorrelation functions $C^p(t)/C^p(0)$ of B_2O_3 at $T = 260°$C are separately plotted (black curves) for each pixel p.
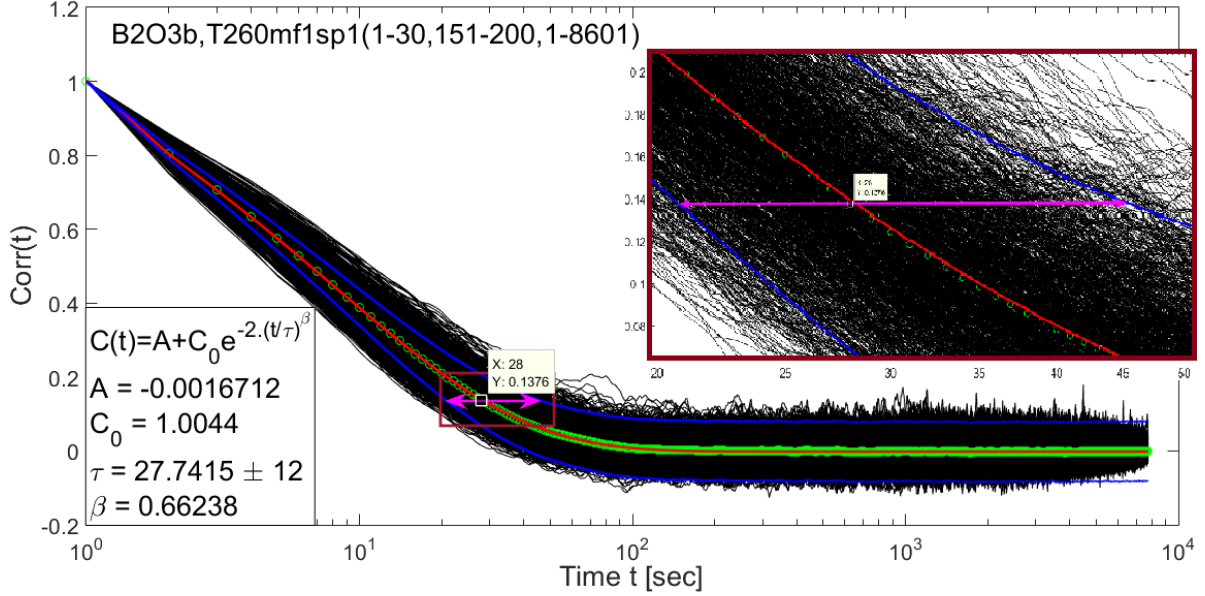

Figure 22: Normalized autocorrelation functions of B_2O_3 at $T = 260°$C separately computed for each pixel

The green circles represent the mean function $\langle C^p(t)/C^p(0)\rangle_p$ averaged over all pixel for each time delay t accordingly to eq.(69). The blue curves show the confidence bands defined by

$$\Delta(t) = \pm\sqrt{\frac{2\tau}{t_{tot}}}[C(0) - C(t)] . \qquad (75)$$

where t_{tot} is the total measurement time. Obviously the uncertainty of $C(t = 0) = \langle I^2\rangle$ at lag $t = 0$ equals zero and increases with lag t. It depends also statistically on the total measurement time in units of the relaxation time τ so that for $C(t) \to 0$ and $C(0) = 1$ we obtain the standard error of the time average

$$\Delta = \pm\sqrt{\frac{2\tau}{t_{tot}}} .$$

Finally the red curve represents the fitted stretched exponential in a good agreement with the mean autocorrelation function $\langle C^p(t)/C^p(0)\rangle_p$. The deviation of the relaxation

time τ is here estimated by the half of the horizontal distance between the confidence bands at $C(\tau)$ which enclose the most curves as shown in the zoomed rectangle on Fig.22.
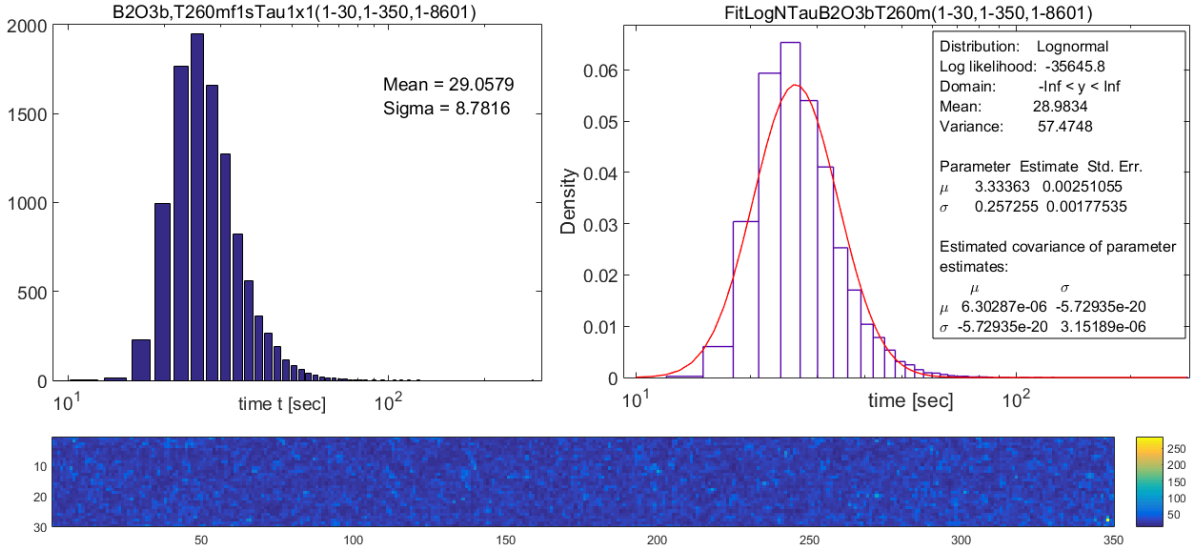

Figure 23: Pixel distribution of the relaxation time τ

This is obviously not the real error of the autocorrelation function that will be later corrected by the number of speckles, but it gives an overview of how the statistics influence the accuracy of our results. It corresponds approximately to the standard deviation of the distribution of τ as represented in Fig.23. On the left picture the histogram of τ is plotted for all pixels on the y-axis against logarithmic x-axis, where the mean value and the standard deviation are directly computed from the data. On the right side the same data is plotted after normalization together with the fitted logarithmic normal distribution function, where μ and σ are the fit-parameters. The deviation of about 8 sec corresponds nearly to the shorter horizontal distance of the left (lower) confidence band from $C(\tau)$ in Fig.22 and the logarithmic shape of the distribution corresponds to the exponential decay of $C(t)$ and its confidence bands.

In an similar way the density distributions of the other two parameters β and C_0 are shown in Fig.24 which appear to be almost normal distributed. In the bottom plots of the figures the spatial distributions of the corresponding parameter are mapped exhibiting the spatial independence (homogeneity) of the parameters.

The so far discussed time averaging method delivers good results only if the measurement is sufficiently long in terms of the relaxation time τ. When in contrast τ increases (e.g. with decreasing temperature) the statistic becomes worse due to the reduced number of temporally independent speckles in the same measurement time. The time averaged intensity will be appreciably up-shifted by the speckle intensities which will remain on for longer time intervals with respect to the total measurement time. In the limit of a
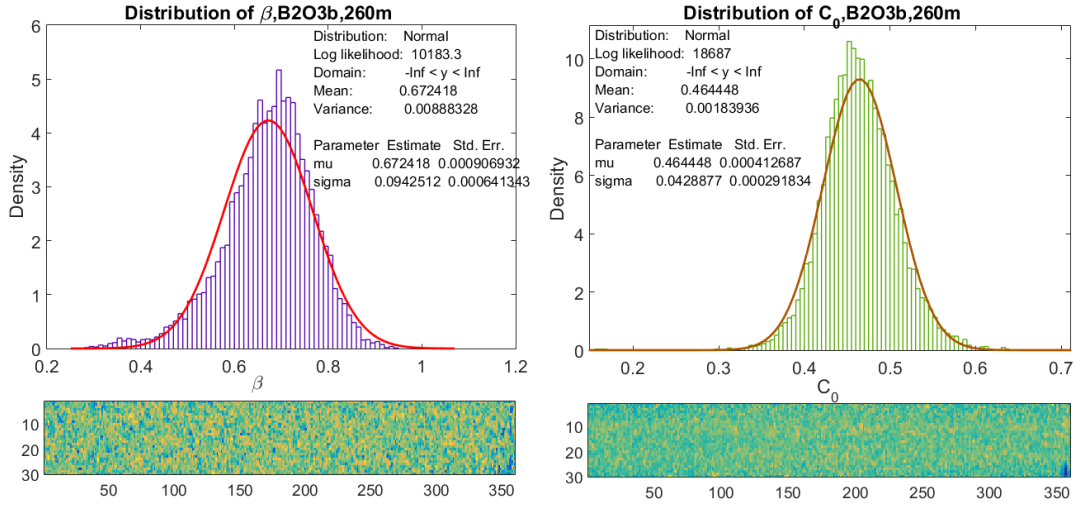
Figure 24: Pixel distribution of the contrast C_0 and the stretching exponent β

glass at low temperature the quasi-static speckle will fluctuate around its "maximum" intensity far above the noise background.
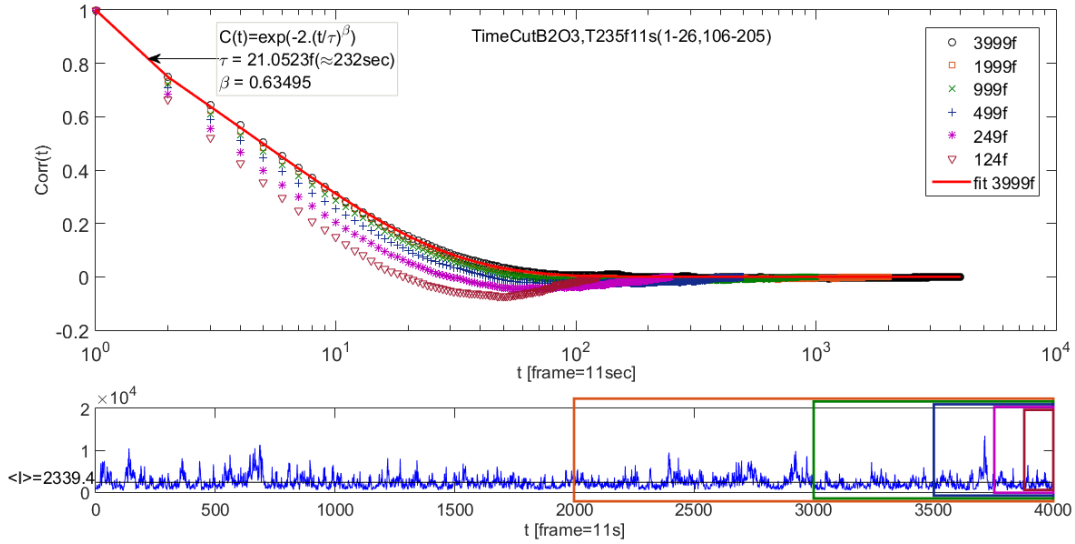

Figure 25: Autocorrelation functions of B_2O_3 at $T = 235°C$ for different integration times

In Fig.25 the autocorrelation functions of B_2O_3 at $T = 235°C$ are plotted. The measurement was performed over 12 hours with an acquisition rate of one frame every 11 seconds. The autocorrelation functions are computed over different integration times (number of frames) each one corresponding to the half of the previous one. In the bottom plot the signal of an arbitrary pixel is plotted to better visualize the time domain used for the average as marked by the coloured rectangles. For the entire measurement time of 3999 frames the mean intensity of the signal is very close to the baseline corresponding to

the mean noise contribution and the autocorrelation function has the expected shape converging for large delays to zero. On the contrary for shorter integration times the data deviates gradually from the real function and the baseline becomes considerably distorted by the spurious mean intensity.
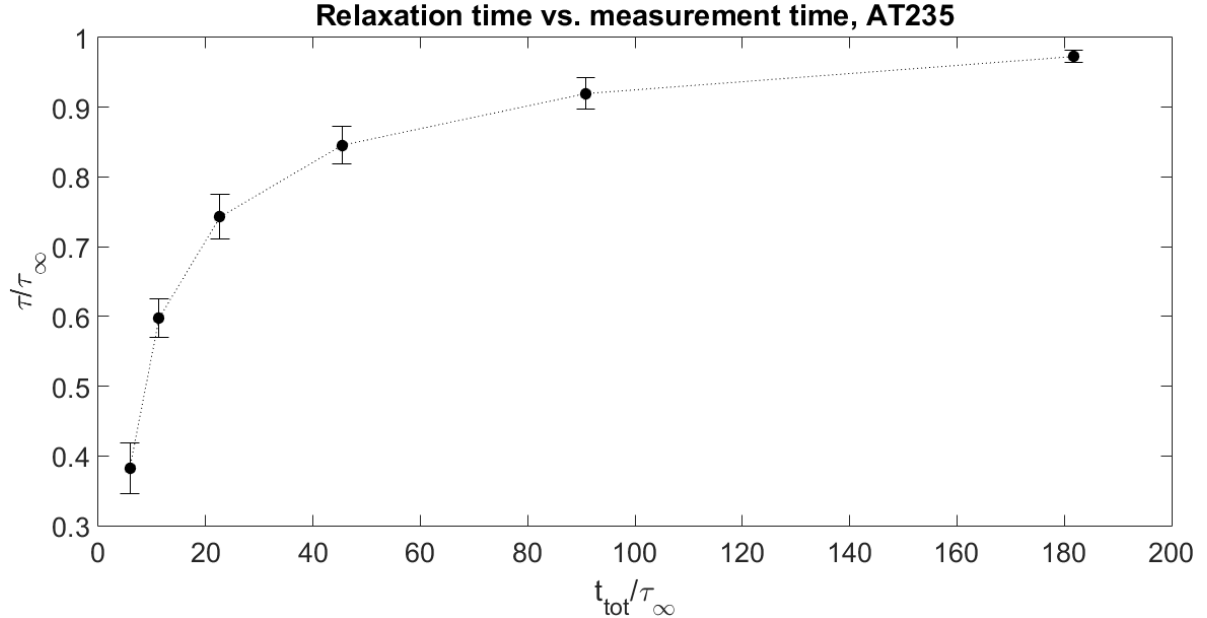

Figure 26: Dependence of the fit parameter τ on the measurement time t

In Fig.26 the dependence of the fit parameter τ on the integration time t_{tot} is plotted as computed by the autocorrelation functions in Fig.25. For long measurements τ approaches asymptotically the real value of the relaxation time $\tau_\infty (\approx 22$ frames in Fig.25). For a measurement of about 100 τ_∞ it deviates already by $\approx 10\%$.

3.3.4 Ensemble average

In the *ensemble averaging* method we simply permute the brackets

$$C(t) = \left\langle \left\langle \frac{(I_f^p - \langle I_f \rangle_p)}{\langle I_f \rangle_p} \cdot \frac{(I_{f+t}^p - \langle I_{f+t} \rangle_p)}{\langle I_{f+t} \rangle_p} \right\rangle_p \right\rangle_f \tag{76}$$

so that we first compute the *ensemble mean* of the correlation coefficients $\langle I(0)I(t) \rangle_p$ then the autocorrelation function averaging over all lags t. Notice please that we first normalize by the ensemble mean intensity of each frame before computing the autocorrelation coefficients. In the ergodic hypothesis the ensemble average is equivalent to the temporal one and independent of the initial time. Substituting the squared time average in the denominator with the ensemble one over each frame in the correlation product we

39

avoid the influence of eventual laser fluctuations or other temporal dependences. More importantly this method has proved to be more suitable for nonergodic systems or as in our case for the nonequilibrium states below the glass transition where τ becomes very large and changes during the measurement.

We consider first the ensemble averaged correlation coefficients

$$C_f(t) = C_{f,f+t} = \left\langle \frac{(I_f^p - \langle I_f \rangle_p)}{\langle I_f \rangle_p} \cdot \frac{(I_{f+t}^p - \langle I_{f+t} \rangle_p)}{\langle I_{f+t} \rangle_p} \right\rangle_p .$$

which define the $f \times f$ square matrix schematically represented in Fig. 27.
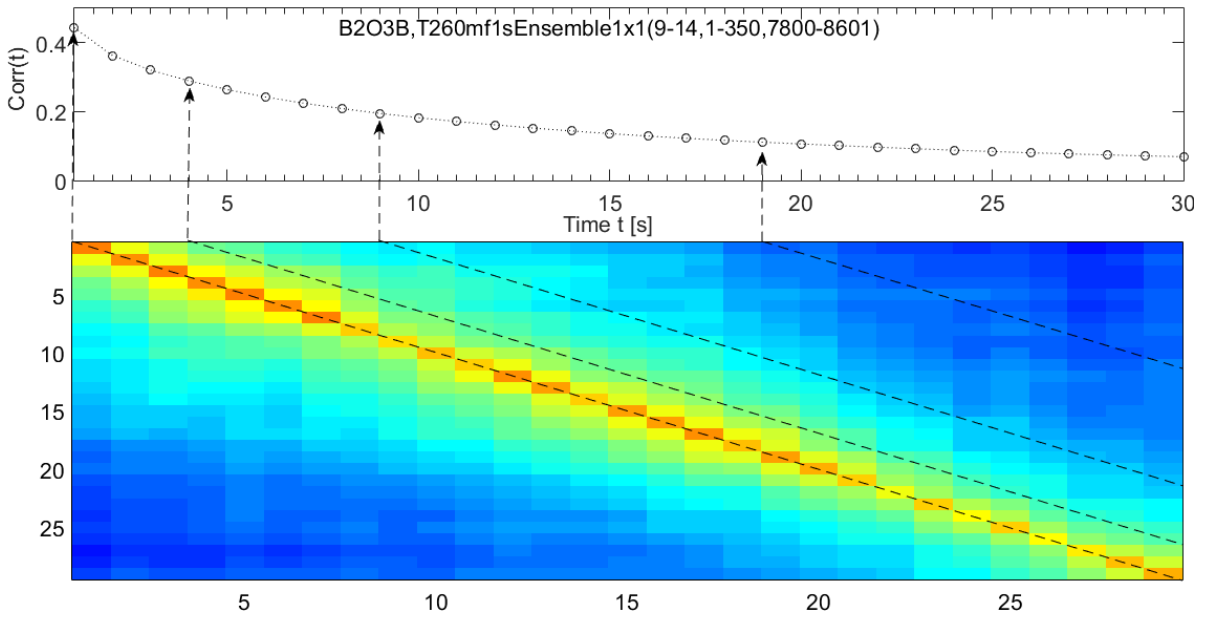

Figure 27: Correlation matrix (bottom) and the corresponding autocorrelation function(top) averaged along the matrix diagonals (dashed lines)

The pixel averaged squared intensities at equal time for each instant f and lag $t = 0$ are clearly visible on the main diagonal (up left to down right) and the correlation function decays with increasing lag t in the direction of the other diagonal (down left to up right). Actually the matrix is constructed by extending the upper right triangle that is naturally defined by positive lags t to a symmetric square matrix. The autocorrelation function $C(t)$ results by averaging along the secondary diagonals from up left to down right for each time delay t as indicated by the dashed lines in Fig. 27.

It is evident that with increasing lag t the number of the corresponding elements decreases until at last for lag $t = N$ (the total number of frames) we will have only one element. Thus the statistical error at longer delays will increase and the autocorrelation curve will fluctuate more and more toward the end. To reduce the influence of such statistical fluctuations on the fitting function the last 10% of the so constructed correlation
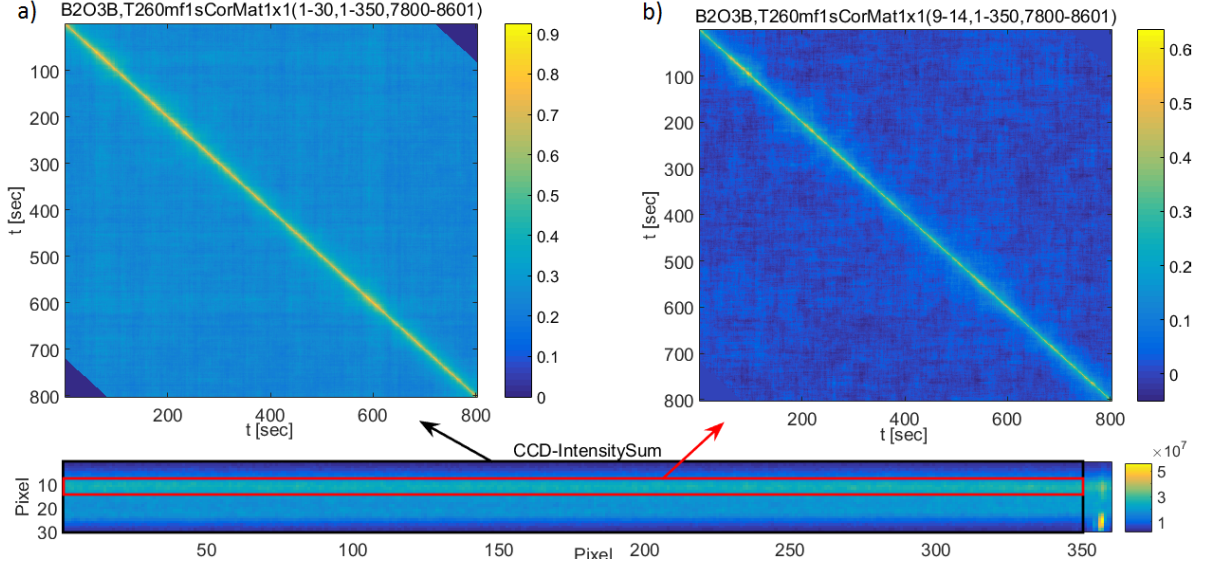
Figure 28: Correlation matrices from two different pixel regions of the same measurement labelled by both black and red rectangles on the intensity map in the bottom image

matrix are excluded in the time averaging and set to zero as a visible reference for the decay of the matrix elements as shown in Fig.28. In fact the upper right and bottom left corners are irrelevant for the function shape.

In the bottom of Fig.28 the map of the time averaged pixel intensities is plotted corresponding to B_2O_3 at $T = 260°$C. Both rectangles indicate the region over which the matrices a) and b) are computed. The correlation matrix a) was constructed by averaging over the almost entire pixel region recorded by the CCD except a small area (> 350) at the right edge where a reflection from the sample walls are visible. The inhomogeneous distribution of the speckle intensities shifts the ensemble mean intensity and results in an up-shifted correlation baseline, this is clearly visible also in Fig.28a) as a strong variation at the corners set to zero. On the contrary the matrix b) was computed over the approximately homogeneous central region indicated by the red (tight) rectangle. Far from the main diagonal it exhibit the expected correlation fluctuations around zero and is hardly distinguishable from the corner value.

The autocorrelation functions of both matrices from Fig.28 are plotted in Fig.29 together with the corresponding fitted exponential functions. The blue squares correspond to the function from the correlation matrix in Fig.28a) and the green circles to that in Fig.28b). The fit parameters τ and β does not differ essentially thus both autocorrelation functions reflect the same dynamic of the sample. However the other two fit parameters the baseline A and the contrast C_0 deviate significantly due to the influence of the beam profile. Using the time averaged pixel intensity shown in the bottom image of Fig.28 to correct
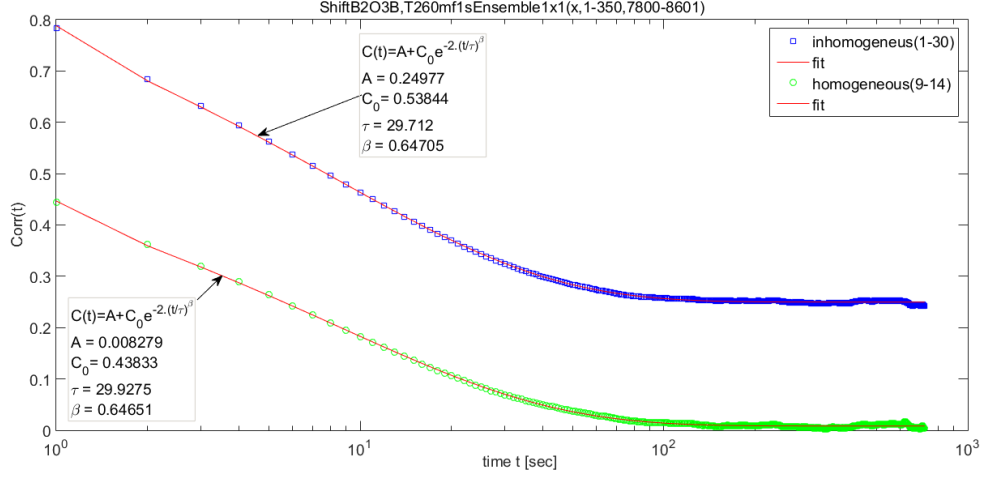
41

Figure 29: Autocorrelation functions of B_2O_3 at $T = 260°$C computed over different pixel regions. The up-shift of the baseline results from the influence of the beam profile

the beam profile led to similar deviations of the autocorrelation function as discussed above by the time averaged method in particular for large relaxation times at temperatures below T_g. Therefore the homogeneous central part of the CCD is considered in what follows.
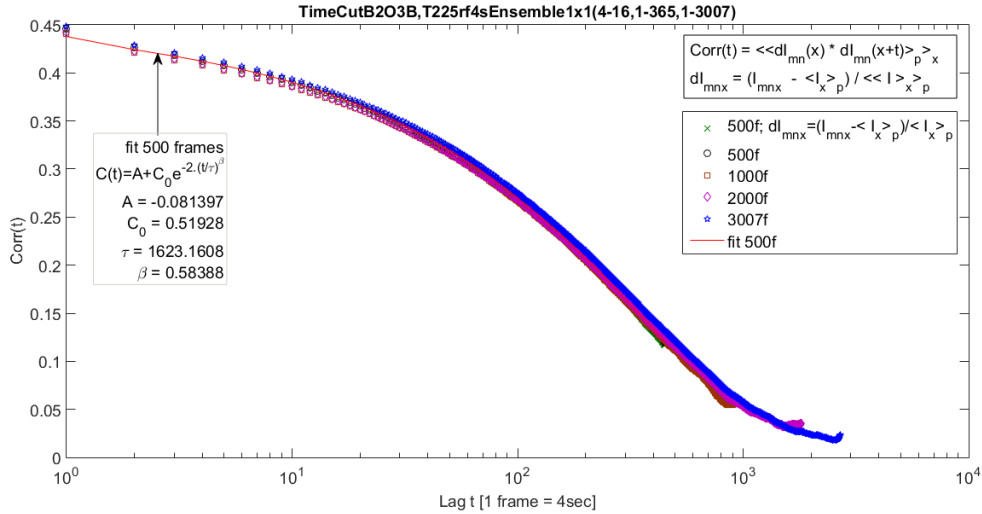

Figure 30: Ensemble averaged autocorrelation functions of B_2O_3 at $T = 225°$C for different integration times.

In Fig.30 the independence of the ensemble averaging method on the integration time is demonstrated. The correlation functions of B_2O_3 at $T = 225°$, thus far below T_g, are computed over 3007, 2000, 1000 and 500 frames with the acquisition rate of one frame every four seconds. All data points coincide well with the fitted exponential curve

(red) although the fit parameters are not very significative due to ageing effects at this temperature (discussed later). Notice please that even for integration times ($\sim 500f$) smaller than the relaxation time ($\sim 1623f$) we obtain reasonable results.

3.3.5 Comparison of the averaging methods

Both methods deliver good results for sufficiently large statistic i.e. long relative integration times and large pixel number. To better estimate the accuracy of the autocorrelation functions we corrected the formula for the confidence bands by the number of coherence areas viewed by the CCD

$$\Delta = \pm\sqrt{\frac{4}{n} \cdot \frac{2\tau}{t_{tot}}}\left(C(0) - C(t)\right) \tag{77}$$

where n is the total number of the considered pixels and the speckle size is approximated to ≈ 4 pixels.

AverageComparison,B2O3A,T235f11s(1-26,1-368,1-3999)

$C(t)=A+C_0 e^{-2\cdot(t/\tau)^\beta}$

$A = 0.211\pm0.006$
$C_0 = 0.4821\pm0.0005$
$\tau = 250 \pm 9$
$\beta = 0.62\pm0.02$

$C(t)=A+C_0 e^{-2\cdot(t/\tau)^\beta}$

$A = -0.0012\pm0.0032$
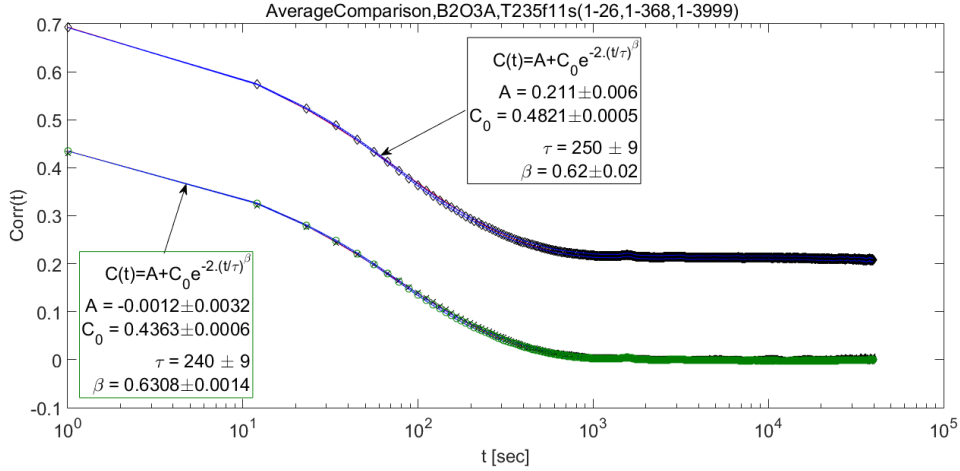$C_0 = 0.4363\pm0.0006$
$\tau = 240 \pm 9$
$\beta = 0.6308\pm0.0014$

Figure 31: Autocorrelation functions computed over the same number of frames and pixels by ensemble (diamonds on top) and time averaging method (circles on bottom). The bottom curve is also superposed on the ensemble average calculated over a small homogeneous pixel region (x-symbols,)

In Fig.31 the autocorrelation functions of the longest (~ 12h) measurement performed at $T = 235°$C are computed using both averaging methods. In order to obtain the same statistic level the maximum pixel number is evaluated including the entire beam profile that led to appreciable shift of the ensemble averaged function baseline $A = 0.21$ and also to rescaling of its contrast factor C_0. As mentioned in the previous section the fit parameters τ and β are not affected by the beam profile and both methods provide consistent values within the estimated half horizontal width of the confidence bands of $C(\tau)$ accordingly to eq.(77). The ensemble averaged autocorrelation function of the flat

central part of the scattered beam (4 by 150 pixels) is represented in the same plot by the black x-symbols coinciding very well with the green circles of the time averaged data.

Although the time averaging method allows to map the spatial distribution of the fit parameters it requires relatively long measurements and provides spurious results for large τ/t_{tot}. Due to the acquisition rate of ~ 1frame/s, most of the measurements have been performed in the vicinity of T_g defined as the temperature where the system has the relaxation time $\tau = 100$s. Therefore the ensemble averaging method was considered as more appropriate and was then used in all following measurements.

3.3.6 Statistical variance

While in the time averaging method we could separately calculate the variance and the standard error of the mean for each fit parameter using the pixel distribution of the autocorrelation functions, in the ensemble average we obtain only one autocorrelation function averaging along the correlation matrix diagonals.
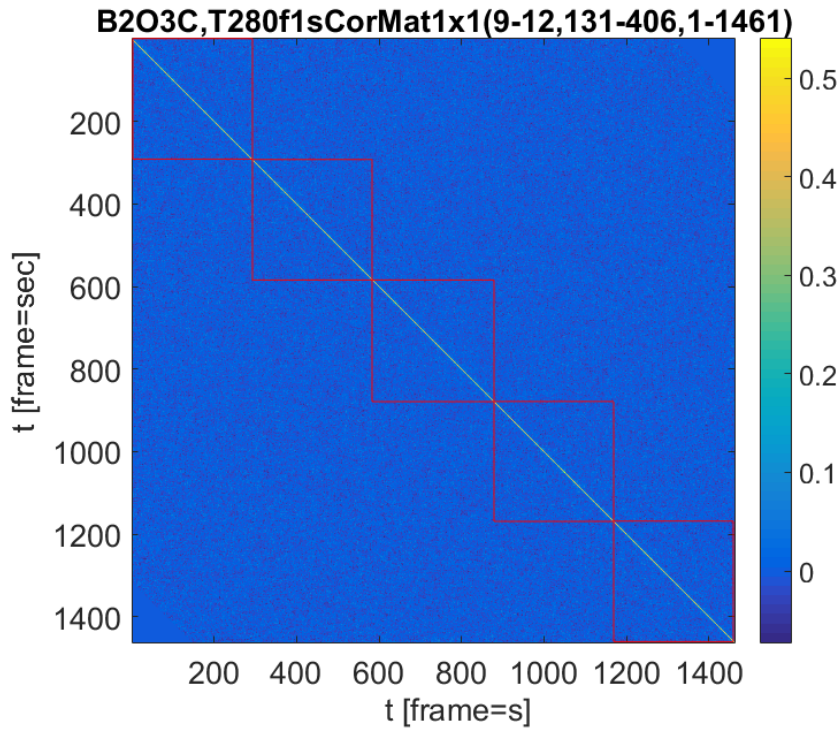

Figure 32: Correlation matrix divided in 5 equal statistically independent submatrices. The data outside the 5 red squares are no more considered

To obtain the statistical variance we divided thus the autocorrelation matrix in equal subregions simulating in this manner many shorter but independent measurements at the

same temperature as shown in Fig.32. Each submatrix corresponds to one independent autocorrelation function of length equal to the submatrix dimension thus we obtain series of n autocorrelation functions of equal length. Obviously the statistics obtained in this manner became worse losing a large amount of data outside the selected subregions and also because the length of a single autocorrelation function becomes much shorter than the total measurement time. However it allows us to study the statistical properties of the results and to derive some conclusions about the behaviour of the system.
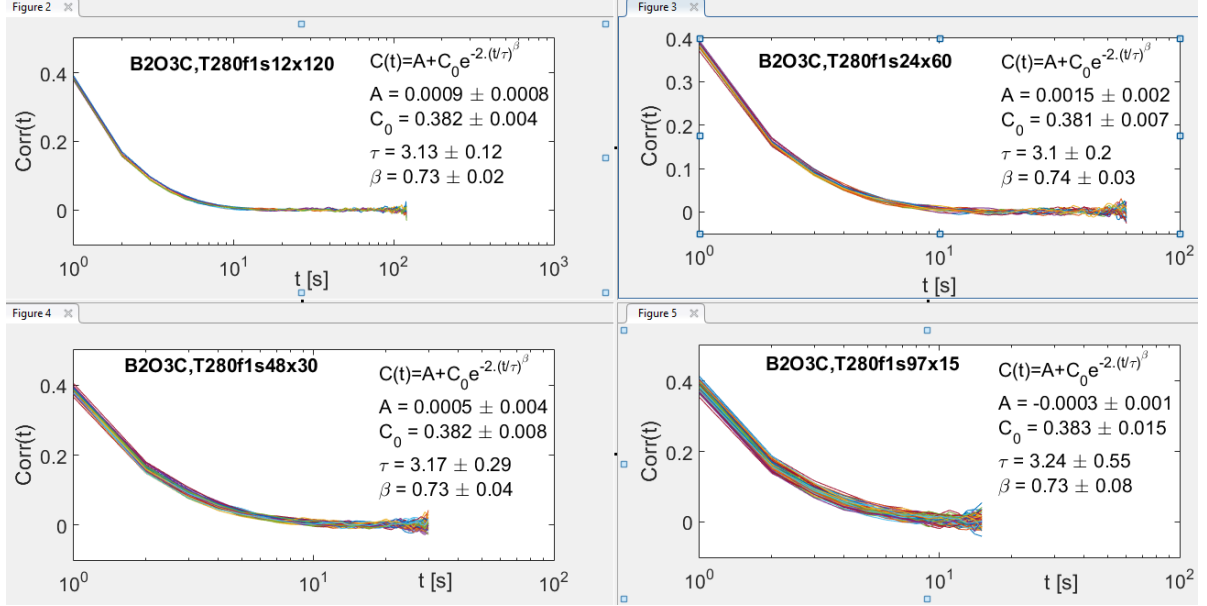

Figure 33: Series of autocorrelation functions of boron oxide at 280°C for 12, 24, 48 and 97 equal correlation subregions of length 120s, 60s, 30s and 15s respectively

Fig.33 shows the autocorrelation function series corresponding to the submatrices obtained by dividing the main correlation matrix into 12, 24, 48 and 97 equal independent square subregions along the main diagonal. The dimensions of the matrices are then 120s, 60s, 30s and 15s respectively. As expected the averaged values of the fit parameters do not differ essentially, but the standard deviations increase significantly reducing the matrix dimension. In Fig.34 the mean values with standard deviations of the fit parameters are plotted versus the length of the autocorrelation functions in units of the relaxation time τ. The baseline $A \approx 0$ is reported only as a reference for the accuracy of the autocorrelation functions and the corresponding fits.

However more interesting is the statistical variance of the parameters that is expected to be proportional to the reciprocal measurement time t. In Fig.35 the relative variances of the relevant τ, β and C_0 are plotted as functions of the reciprocal time in units of τ. As expected the variances of all three parameters increase linearly with decreasing measurement time. More important in the limit $t \to \infty$ the variance seems to vanish (within the fit errors) suggesting thus a dynamical homogeneity of boron oxide at 280°C.
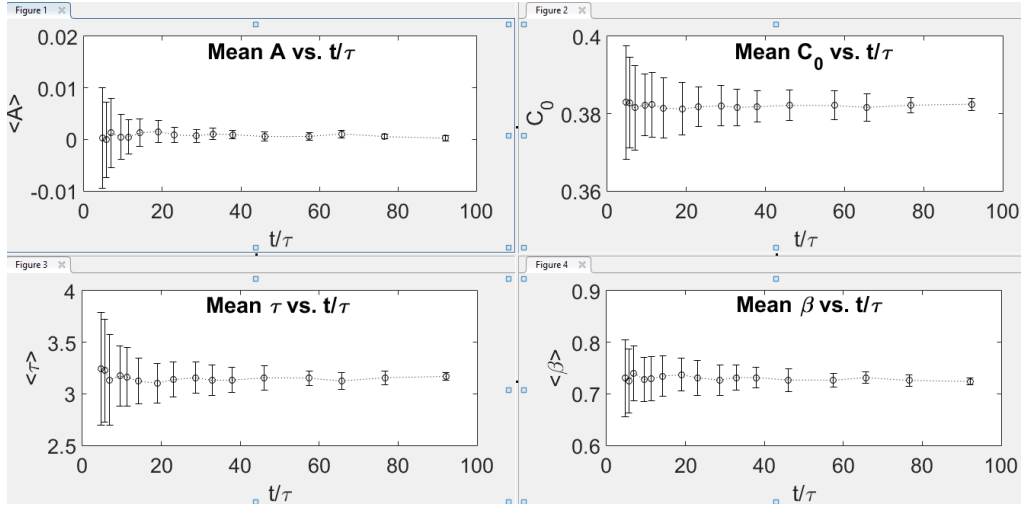
Figure 34: Averaged fit parameters with standard deviations in dependence on the length of the autocorrelation functions

If instead the intercepts (P2) in Fig.35 would be positive non zero constants it would indicate a non statistical variance contribution caused by dynamical heterogeneities as proposed by Duri et al [Dur05]. The tendency of the intercepts to small negative values (within the errors) could be explained by the uncertainty of the autocorrelation fits which increases with increasing ratio τ/t. This is well visible in particular by the variance of τ which has distinctly higher values for integration times $t < 10\tau$. On the contrary the variance of the contrast follows quite strictly the $1/t$-proportionality because C_0 is simply the average squared intensity of the measured signal thus independent of the autocorrelation fit.
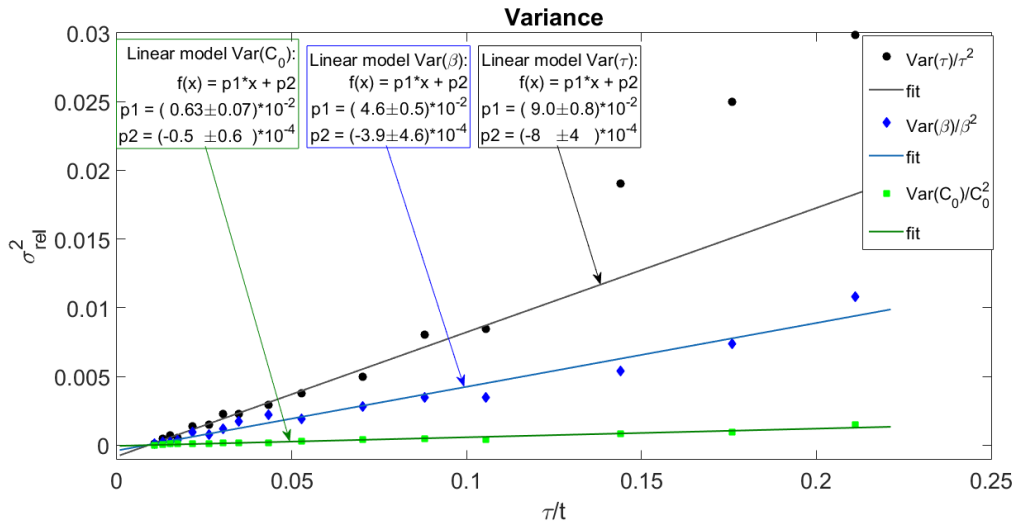

Figure 35: Variances of τ, β and C_0 depending on the measurement time t

3.4 Results

3.4.1 Temperature dependence

Light scattering measurements were performed on three different samples of B_2O_3 at various temperatures in the vicinity of T_g. In Fig.36 the autocorrelation functions of sample C are plotted at different temperatures covering the temperature range measured by the CCD. Notice please the logarithmic scale of the x-axis that indicates the rapid change in the viscosity ($\sim$relaxation time) for small variation of the temperature. The green squares correspond to the relaxation time of about 100s defining thus the glass transition temperature at $T \approx 250°$C. The data on the left side of the green squares correspond consequently to the supercooled liquid domain and on the right rather to the solid glass where at 230°C (brown triangles) ageing effects have also been observed (to be discussed below).
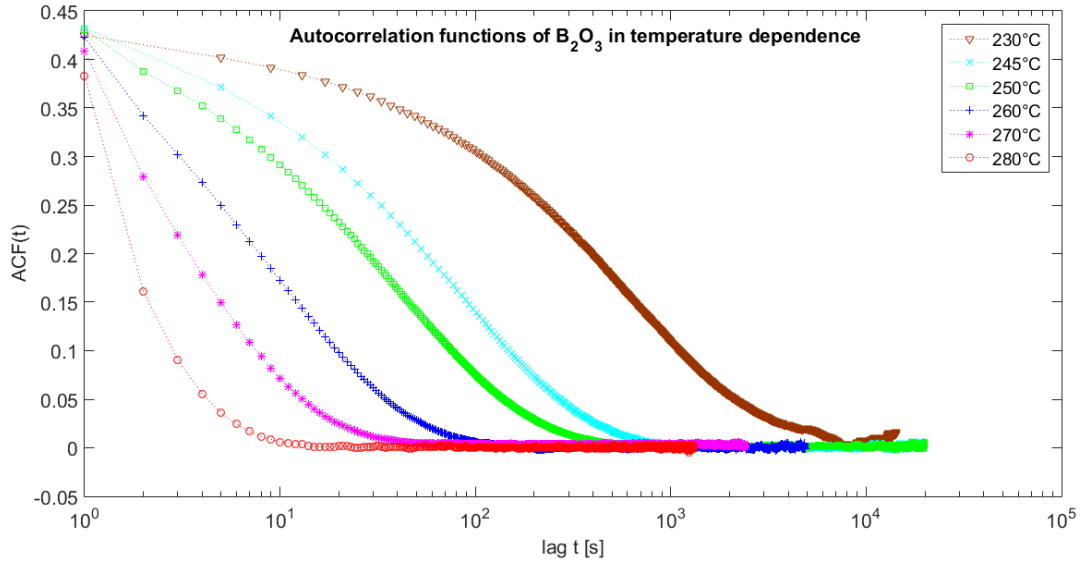

Figure 36: Autocorrelation functions of B_2O_3 in temperature dependence

It is remarkable that the amplitude of most autocorrelation functions in Fig.36 starts from nearly the same value of $C_0 \approx 0.43$ except for those with relaxation times $\tau < 10$s.

For each autocorrelation function we are able to fit the stretched exponential function

$$C(t) = C_0 \cdot e^{-2(t/\tau)^\beta}$$

and plot the fit parameters C_0, τ and β as functions of the temperature. The non ergodicity level f_0 of each autocorrelation function has been calculated according to

$$f_0 = \sqrt{\frac{C_0}{A_{coh}f_{st}}}$$
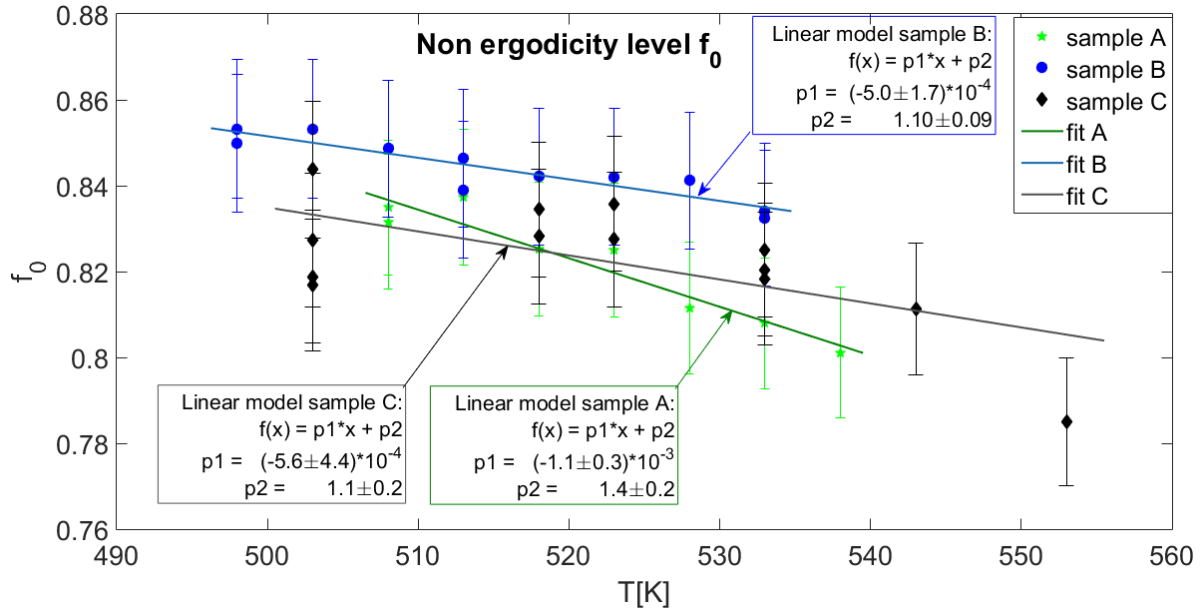
as introduced in section 3.3.2.

Figure 37: Non ergodicity level f_0 at different temperatures

The behaviour of f_0 at different temperatures is shown in Fig.37. All three samples exhibit the similar slight decrease with increasing temperature and approximately same values within the error bars. Remarkable are the outlier points of sample C at the higher temperatures 553K(280°C) and 543K(270°C) as well as those at 503K(230°C). The former appears lower than expected from the trend suggesting the presence of possible systematic errors related to the fact that at higher temperatures we don't reach the plateau of the correlation function at short times. The points at 503K are probably influenced by ageing effect as they are taken from the corresponding measurements on an ageing glass discussed later. It is also noticeable that the slope of f_0 of sample A appears to be two times larger than those of the other two samples. This can be explained by the different preparation history of sample A described in section 3.1. As we will see below the temperature behaviour of the other two parameters β and τ of sample A differs also from those of samples B and C.

The dependence of the stretching exponent β on the temperature is reported in Fig.38. The slight increase of β with the temperature confirms the behaviour observed also by Sidebottom et al. [Sid93] although the slope of our data appears to be about two times higher. However the temperature range of our measurements is significantly smaller than that by Sidebottom et al. and the variance of the data is relatively large resulting into errors of 30%-50% for the fitted slope. Once again we see that the behaviour of sample A differs from those of B and C and the data points at the boundary temperatures 553K, 543K and 503K of sample C deviate a little bit from the general trend as mentioned above.
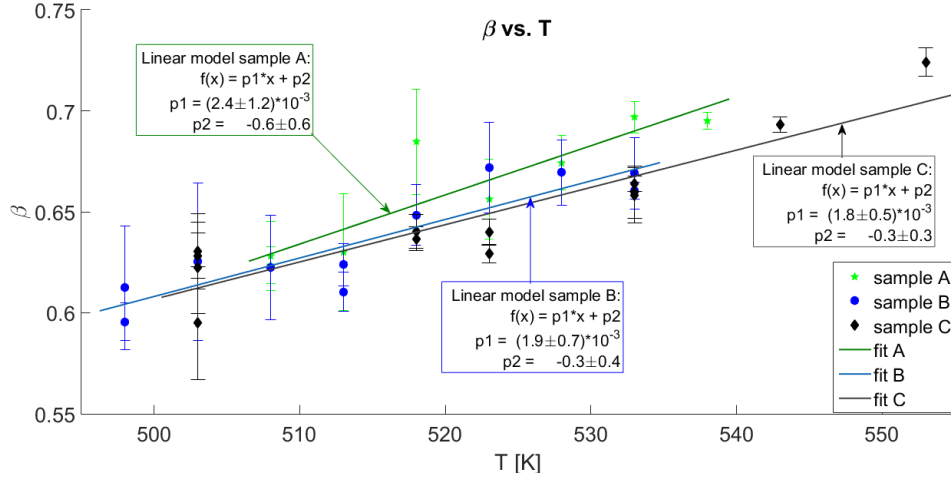
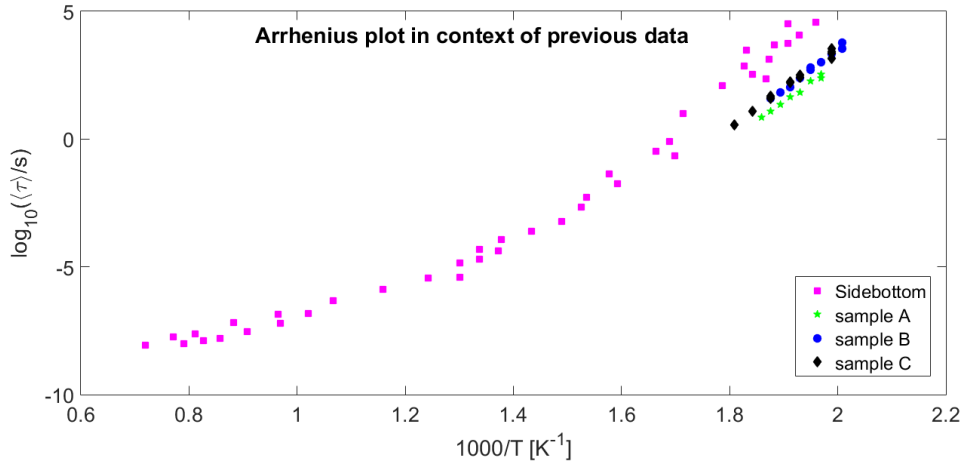Figure 38: Stretching parameter β as a function of temperature

Figure 39: Relaxation time τ as a function of temperature

The behaviour of the mean relaxation time $\langle\tau\rangle$ is shown in Fig.39. Accounting for the fact that the fitted stretched exponential is an empirical approximation for the sum over many relaxations, the mean relaxation time is here given by

$$\langle\tau\rangle = \frac{\tau}{\beta} \cdot \Gamma(\frac{1}{\beta})$$

where $\beta(\approx 0.65)$ is the stretching exponent discussed above. The y-axis is logarithmic scaled exhibiting the expected exponential dependence of $\langle\tau\rangle$ on the temperature as given by Vogel-Fulcher law

$$\tau(T) = \tau_0 e^{\frac{B}{T-T_0}} \ .$$

All samples have approximately the same slope that is related to the fragility index discussed below. The magenta squares show the data reported by Sidebottom et al. [Sid93]. The corresponding glass transition temperatures $T_g(\tau = 100s)$ of each sample

are directly interpolated from Fig.39. Sample A indicates a different glass transition temperature $T_g^A \approx 514$K that is about 10K lower than $T_g^B \approx T_g^C \approx 524$K of samples B and C respectively. This fact can be explained by the probably higher water (OH^-) content in sample A that leads to reduced glass transition temperature of B_2O_3 as reported by Ramos et al [Ram96]. As described in section 3.1 the sample A was held only 12 hours at $900°$C whereas samples B and C 48 hours. We suppose thus that the adsorbed humidity in sample A was not fully evaporated. However, we could not quantitatively measure the water content of the samples, that was reported by Ramos et al. to cause differences in T_g of $10-30$K for OH^--concentrations of $3.4-5.8$ mol%.
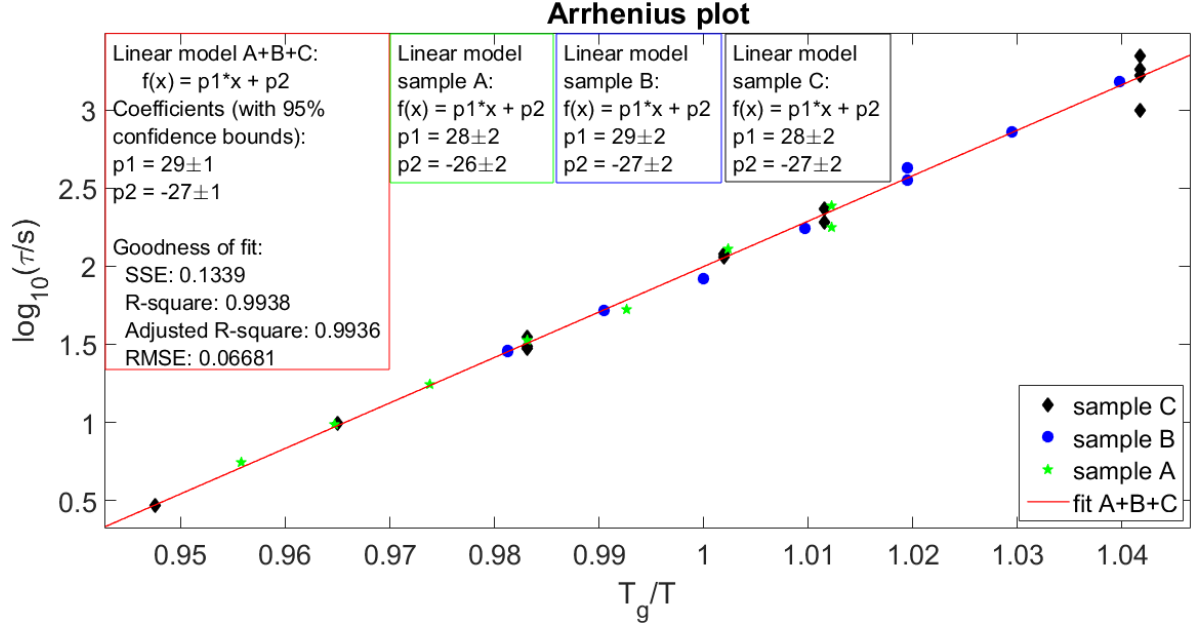

Figure 40: Arrhenius plot of the relaxation time τ of the three different samples of B_2O_3

Finally plotting $\log_{10} \tau$ versus the reciprocal temperature in units of T_g as shown in Fig.40 we obtain the fragility index $m = 29 \pm 1$ of boron oxide given by the slope of the red line. The data points of all samples coincide well with the fit line except for the points of the ageing sample C at 503K in the upper right corner. For the sake of clarity only the fit line is plotted, which accounts for the data points of all samples, but in the coloured text boxes the fit parameters for each sample are separately reported. There is no significant difference in the fragility of the different samples which all coincide within the errors also with the value $m = 27 \pm 3$ reported by Sidebottom et al. [Sid07]

3.4.2 Ageing

The properties of a non-equilibrium system continuously change in time as the system evolves to its equilibrium configuration. Initially the changes occur faster but approaching the equilibrium state the dynamic becomes progressively slower. Thus the autocorrelation function depends not only on the relaxation time but also on its *ageing*, i.e. the waiting time after the system was subjected to an external conditions change (as the temperature variation). To observe such ageing effects we measured continuously the relaxation time of B_2O_3 starting at $T = 270°C$ and quenching it to $T = 230°C$. The measurement was then repeated in the next two days while the sample has been kept at constant $T = 230°C$.
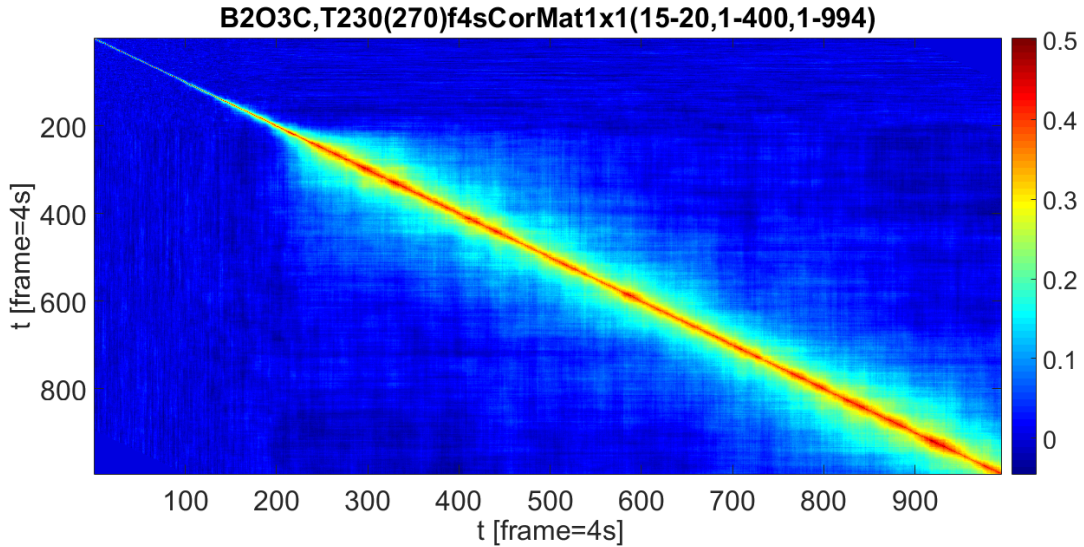

Figure 41: Correlation matrix of B_2O_3 while quenching it from $T = 270°C$ to $T = 230°C$

The correlation matrix corresponding to the quenching process from $T = 270°C$ to $T = 230°C$ is plotted in Fig.41 with the rate of 1 frame every 4 sec. The furnace needed about 15min to achieve $T = 230°C$ that is well visible in the first ≈ 200 frames. After that the system, initially liquid at $T = 270°C$, is solidified at $T = 230°C$. While the system is ageing we expected a similar visible "widening" of the main diagonal as by the initial quenching process. Thus we continued the same measurement for about 6 hours in total. The correlation matrix of the next 5 hours, when the system is supposed to have equilibrated at $T = 230°C$ is reported in Fig.42. Because there are no directly visible effects we conclude that this process occurs on a much longer time scale relative to the relaxation times. Thus we repeated the measurement without changing anything in the next two days.

In Fig.43 the autocorrelation functions of the ageing B_2O_3 are plotted at different ages. The red crosses and dark red circles in the picture represent the data recorded during
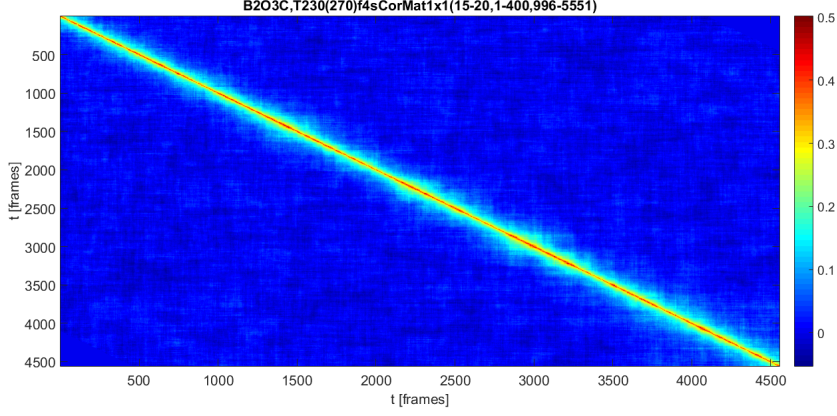
Figure 42: Correlation matrix of B_2O_3 at $T = 230°C$ one hour after quenching it from $T = 270°C$

the quenching process within the initial $\approx$ 15min of the measurements and are shown as a reference for the rest of the data which are considered to be equilibrated at $T = (230 \pm 0.1)°C$. In consideration of the logarithmic scaled time axis we see that the autocorrelation function unambiguously changes and the relaxation time increases up to 3 times the initial $\tau \approx 800s$. It seems also that the contrast C_0 changes slightly to higher values as the glass ages. However, there are not enough data points and the uncertainty of C_0 is relatively high to make conclusions on its behaviour.
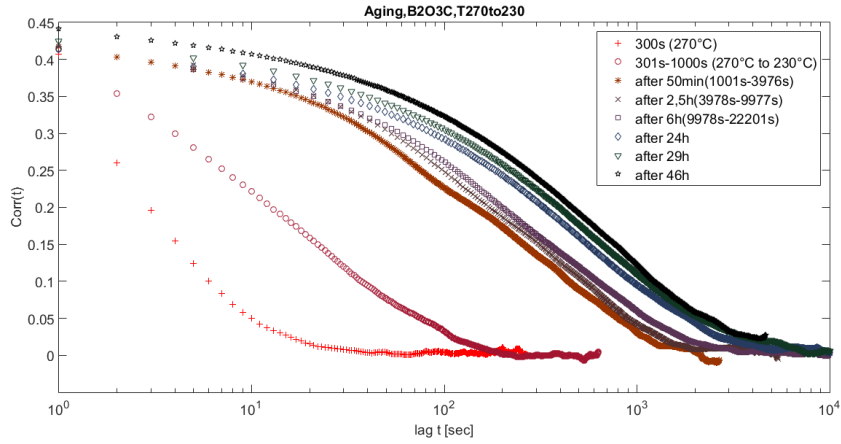

Figure 43: Autocorrelation functions of ageing B_2O_3 at $T = 230°C$. The red crosses and dark red circles are the autocorrelation functions computed over the first 15 min during the quenching process initiated at $T = 270°C$

The dependence of the relaxation time τ on the waiting time after the glass has formed is reported in Fig.44 where the errors of τ are estimated individually for each autocorrelation function as described above and the uncertainties in the ageing times correspond simply to the measurement durations. Paluch et al. described the ageing of CKN by

52

the stretched exponential function

$$\tau_\sigma(t) = A \exp\left[-\left(\frac{t}{\tau_{age}}\right)^{\beta_{age}}\right] + \tau_\infty$$

where $\tau_\sigma(t)$ is the relaxation time of the conductivity σ depending on the ageing time t and $A, \beta, \tau_{age}, \tau_\infty$ are constants [Pal13]. However we could not fit this function to the few data points we have, but they indicate a similar trend to approach a certain value τ_∞ starting at a value fixed by A.
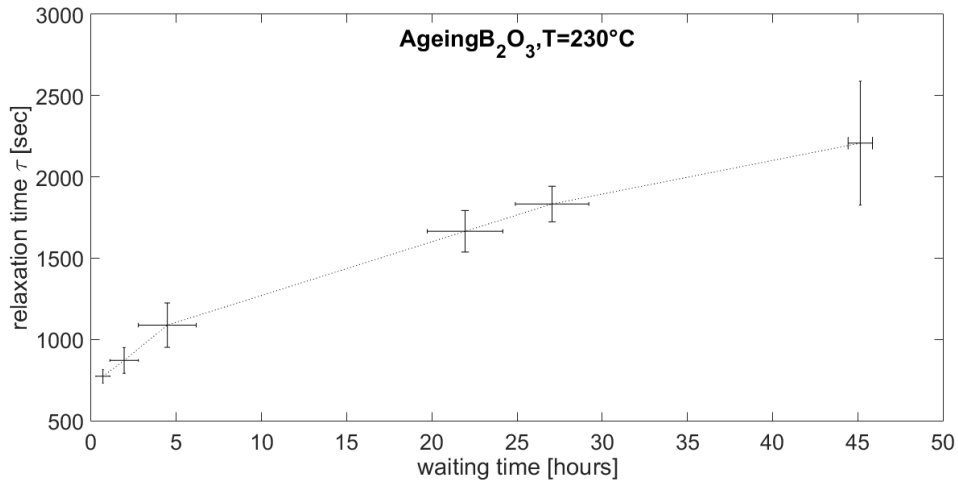

Figure 44: Relaxation time of ageing B_2O_3 at $T = 230°C$

4 Conclusions

A multi-speckle setup based on a CCD-camera has been installed and optimized to measure dynamic light scattering on samples close to the structural arrest. This setup provides speckle sizes of nearly 4 pixels in size. This choice has the advantage of granting the maximum contrast of the calculated autocorrelation functions. To improve the statistics it may be better to use smaller speckles of about one pixel size. This would, however, also reduce the contrast (amplitude) of the computed autocorrelation functions. The compromise between contrast and statistics is a non-trivial issue in particular for low scattered intensity as in the case of the present study.

Two different methods for processing of the raw data have been investigated and compared. Both methods, based on the computation of the autocorrelation function, provide consistent results for ergodic systems and for sufficiently long measurements, but differ essentially at temperatures close to and below T_g, where the system is arrested in a non-equilibrium state. The *time averaging method* allows to separately calculate the autocorrelation function of each pixel and to map the spatial distributions of the observed quantities. It provides good results for autocorrelation functions averaged over many relaxation times ($> 100\tau$), but it is not very suitable to study systems close to or in the arrested state, where in particular spatial and temporal dynamical heterogeneities can be expected. We have shown the systematic deviation of the relaxation time τ measured using the time averaging method as a function of the integration time (Fig.26) and propose that this result can be further used as a correction factor for insufficiently long integration times. This can be particularly useful when a pixel mapping of the relaxation times is of interest.

On the other hand the *ensemble averaged* autocorrelation function doesn't distinguish among different pixels, but it yields, depending on the pixel number, precise results regardless of the measurement time. The correlation matrix described in section 3.3.4 provides moreover features allowing to study higher correlation moments and time resolved heterogeneous dynamics as proposed by Duri et al.[Dur05]. Improving the statistics of the exploited pixels, e.g. by reducing the speckle size as mentioned above, but also using techniques for correction of the intensity profile of the scattered beam, it will allow investigating different regions of interest (ROI) of the CCD and studying spatial correlation and heterogeneity as well [CW10].

We studied the statistical distributions and variances of the measured quantities. The measured intensity distribution of the speckle pattern yields an estimate of the background intensity by comparison with the predicted theoretical distribution [DC15]. This may be useful to extract the stray light contribution, that is not always directly measurable. The variances of the correlation parameters suggest some conclusions on the dynamical heterogeneity of the considered system. The dynamics of supercooled liquid boron oxide at 553K appears to be homogeneous within the statistical accuracy provided

by an integration time of $10^4 \cdot \tau$ and for a CCD-area of ≈ 280 speckles sizes. That means that eventual dynamical heterogeneities at 553K could be observable only pushing the statistics to more than $10^4 \times 280$ independent coherence events. However, these studies should be extended to lower temperatures close to T_g, where the dynamical heterogeneity should become observable.

We have determined the glass transition temperatures $T_g^A \approx 514$K and $T_g^{B,C} \approx 524$K of our B_2O_3-samples A, B and C respectively, which are comparable with T_g-values from previous works [E.R93, Sid93, Ram96]. The published values of T_g vary in the range from 524K [Sid93] up to 580K [Bot07] strongly depending on the purity as well as on the preparation method as reported by Ramos et al.[Ram96]. Consequently our autocorrelation parameters, namely the relaxation time τ, the non ergodicity level f_0 and the stretching exponent β and their temperature dependences slightly differ from sample to sample. The fragility $m = 29 \pm 2$ of our samples, instead, appears to be independent of T_g and is in a good agreement with the value $m = 27 \pm 3$ reported by Sidebottom at al.[Sid07].

We reported τ, β and f_0 as function of temperature T. The relaxation time exhibits the expected exponential dependence on T. Our results for the observed slight increase of β with T are consistent with the results of Sidebottom et al.[Sid93]. The slight decrease of f_0 instead may be influenced by the insufficient frame rate of ≈ 1 Hz of our CCD. Therefore it would be worthy to study the non ergodicity level using a CCD with a higher frame rate or at lower temperatures, i.e. where the relaxation time gets longer and the initial plateau $\sim f_0^2$ of the α-relaxation is well defined. Our mean value of $f_0 = 0.84 \pm 0.3$ is higher than the (constant) value of 0.75 ± 0.03 reported by Sidebottom et al. [Sid07]. This discrepancy could be related to our estimation of the stray light factor f_{st} in section 3.3.2, which was supposed to be temperature independent and equal in both CCD and photomultiplier data. However more studies should be carried out to test this hypothesis.

In the last part of the thesis the ageing of B_2O_3 -glass is observed and the relaxation time is reported as a function of the ageing time. For B_2O_3 this phenomenon appears at relatively large time scales (the measurements were carried out over three days) so that we could measure only few ageing points. The variation of the relaxation time τ with the waiting time is well visible starting at a certain fixed point τ_0 and increasing up to a saturation value τ_∞.

The whole set of results obtained in this thesis work, both the instrumental, the data-analysis related and the scientific ones, open the way to new studies on glass-formers close to the structural arrest, where the multi-speckle light-scattering setup can be exploited to obtain new information with high-statistical accuracy on the nature of the glass-transition process.

References

[BD74]   J. A. Bucaro and H. D. Dardy. Light scattering from boron trioxide through the glass transition. In *Journal of Applied Physics 45, 2121.* 1974.

[Bot07]   W.J. Botta. Glass transition, thermal expansion and relaxation in B_2O_3 glass measured by time-resolved X-ray diffraction. In *Journal of Non-Crystalline Solids 354 (2008) 325–327.* 2007.

[BP76]   Bruce J. Berne and Robert Pecora. *Dynamic light scattering.* 1976.

[CR05]   Luca Cipelletti and Laurence Ramos. Slow dynamics in glassy soft matter. In *J. Phys.: Condens. Matter 17 R253.* 2005.

[CW99]   Luca Cipelletti and D. A. Weitz. Ultralow-angle dynamic light scattering with a charge coupled device camera based multispeckle, multitau correlator. In *REVIEW OF SCIENTIFIC INSTRUMENTS VOLUME 70, NUMBER 8.* 1999.

[CW10]   Luca Cipelletti and Eric R. Weeks. Glassy dynamics and dynamical heterogeneity in colloids. In *arXiv:1009.6089v1.* 2010.

[DC15]   Aristide Dogariu and Remi Carminati. Electromagnetic field correlations in three-dimensional speckles. In *Physics Reports 559 (2015) 1–29.* 2015.

[Deb01]   Pablo G. Debenedetti. Supercooled liquids and the glass transition. In *Nature vol 410.* 2001.

[Dur05]   Agnès Duri. Time-resolved-correlation measurements of temporally heterogeneous dynamics. In *PHYSICAL REVIEW E 72, 051401.* 2005.

[Ell00]   Stephen Elliott. *The physics and chemistry of solids.* 2000.

[E.R93]   E.Roessler. Low-frequency Raman scattering on different types of glass formers used to test predictions of mode-coupling theory. In *Physical review B, vol.49, nr.21.* 1993.

[Fon15]   Prof. Aldo Fontana. Lecture on physics of disordered systems at the University of Trento, 2015.

[Nga93]   Kia L. Ngai. Nonexponential relaxation in strong and fragile glass formers. In *The journal of chemical physics.* 1993.

[Pal13]   M. Paluch. Heterogeneous dynamics of prototypical ionic glass CKN monitored by physical aging. In *PHYSICAL REVIEW LETTERS 110, 015702*. 2013.

[Ram96]   M.A. Ramos. Correlation of elastic, acoustic and thermodynamic properties in B_2O_3 glasses. In *Journal of Non-Crystalline Solids 221 1997 170–180*. 1996.

[RC05]   David R. Reichman and Patrick Charbonneau. Mode-coupling theory. In *arXiv:cond-mat/0511407v1*. 2005.

[Sid93]   D. Sidebottom. Two-step relaxation decay in a strong glass former. In *PHYSICAL REVIEW LETTERS,VOLUME 71, NUMBER 14*. 1993.

[Sid07]   D. L. Sidebottom. Connecting structure and dynamics in glass forming materials by photon correlation spectroscopy. In *PHYSICAL REVIEW B 75, 132201*. 2007.

[Whi73]   G K White. Thermal expansion of reference materials: copper, silica and silicon. In *J. Phys. D: Appl. Phys. 6 2070*. 1973.

[Wik08]   Wikipedia. https://en.wikipedia.org/wiki/viscosity, 2008.

[WW93]   Apollo P. Y. Wong and P. Wiltzius. Dynamic light scattering with a CCD camera. In *Review of Scientific Instruments, Volume 64, Issue 9*. 1993.

[Zar82]   Jerzy Zarzycki. *Les verres et l'ètat vitreux*. 1982.

Aknowledgments

I thank Prof. Dr. van Loosdrecht for helping me by words and deeds, for his never-ending support and warm encouragement.

I thank Prof. Dr. Monaco for giving me the opportunity to write this diploma Thesis at the University of Trento and for his expert guidance and professional advice.

I would also like to thank Prof. Dr. Fontana for his qualified support and who was also a great source of motivation throughout the many conversations we had.

I would like to extend great thanks to the entire research team of Prof. Dr. Monaco who readily and willingly provided me with information at any time.

I thank my lovely wife for trusting me, for her patience and continued support.